



# OPEN Risk identification and assessment for multitype safety events under the coupling of environmental factors

Qian Liu<sup>1</sup>, Junqiao Li<sup>1</sup>✉ & Zhixin Jin<sup>1,2</sup>

In high-risk industrial settings, the proliferation of sensor data provides crucial support for fundamental research on safety events (SEs) and for precise risk analysis. However, existing data-driven methods struggle to reveal the nonlinear couplings among multiple factors and lack a systematic framework to explain how these factors jointly contribute to different types of SEs. To address these limitations, this study proposes a theory–data integrated model for multitype SE risk identification and assessment. From a cross-scale emergence perspective, the study elucidates that SEs arise from a chain-evolution process driven by the nonlinear coupling of diverse environmental factors and constructs a theoretical framework describing hierarchical factor associations and cross-scale interactions. Building upon this theoretical foundation, a data-driven risk identification and assessment model (RIAM) is established. This model quantifies the contributions of measurable environmental factors (MEFs) that significantly influence SEs through online learning. Experimental results demonstrate that the proposed model effectively captures the cumulative risk effects arising from multi-factor coupling, thereby enhancing both event identification accuracy and model interpretability. This study provides a novel perspective and methodological foundation for SE prediction and integrated prevention in complex industrial environments.

**Keywords** Safety events, Environmental factors, Contribution, Cross-scale emergence, Risk assessment, Interpretability

In complex production systems, heterogeneous safety events (SEs) often co-occur and interact, with their emergence shaped by the nonlinear coupling and dynamic evolution of multiple environmental factors. A comprehensive investigation of inter-factor interactions and inter-event coupling is therefore pivotal for accurate SE identification and early-warning prediction<sup>1</sup>. With the advent of big-data technologies, multi-source environmental datasets have opened new avenues for the study of SEs, while simultaneously posing new challenges to conventional analytical approaches.

Safety theory models provide the theoretical foundation of the logical relations among factors in production systems and the mechanisms by which events are triggered. Constrained by prevailing technological conditions, traditional models often rely on limited samples and simplified assumptions<sup>2,3</sup>. These models typically adhere to established paradigms and interpret causal mechanisms from a static, qualitative standpoint. Consequently, they remain inadequate for characterizing inter-factor interactions and nonlinear coupling mechanisms in complex systems when confronted with high-dimensional, dynamic, and multi-source environmental data<sup>4</sup>. Therefore, it is essential to reframe safety theory from a new perspective that integrates systemic principles with data-driven intelligence and captures the dynamic evolution of events in complex production systems.

The introduction of data has provided new paradigms and methodological foundations for theoretical research in safety science. Scholars have attempted to model the causal mechanisms and evolutionary processes of SEs using big data analytics. For instance, Huang et al.<sup>2</sup>, Wang et al.<sup>5,6</sup>, and Jin et al.<sup>7,8</sup> proposed big data-driven frameworks for SE analysis, opening new perspectives for studying safety mechanisms in complex systems. Nevertheless, current big data-based theories still fall short of elucidating how heterogeneous factors jointly contribute to SE occurrence. One key reason is that many existing studies continue to treat risk factors as isolated variables under static settings, thereby overlooking interdependencies among multiple threats and the

<sup>1</sup>College of Safety and Emergency Management Engineering, Taiyuan University of Technology, Jinzhong 030600, China. <sup>2</sup>Center of Shanxi Engineering Research for Coal Mine Intelligent Equipment, Taiyuan University of Technology, Taiyuan 030024, China. ✉email: lijunqiao@tyut.edu.cn

influence of dynamic response mechanisms<sup>9</sup>. This limitation constrains both the understanding of the intrinsic mechanisms of SEs and the effective utilization of factor state data. In fact, the evolution of SEs essentially results from the complex interactions among multiple factors. These factors continuously evolve across spatial and temporal dimensions, and their state changes collectively drive the occurrence and evolution of SEs. Therefore, it is necessary to further explore the interrelationships among these factors and their underlying causal mechanisms influencing SEs, to better provide theoretical explanations and modeling pathways for nonlinear safety phenomena in complex systems.

Similarly, the advancement of big data technologies has enabled the development of more refined and accurate risk assessment models<sup>10</sup>. In complex production systems, different types of SEs often overlap and transform, exhibiting coupling-induced disaster evolution characteristics<sup>11,12</sup>. Therefore, these SEs may share similar causal factors and underlying principles. However, existing risk assessment methods are generally developed for individual SEs in isolation<sup>10,13,14</sup>. Although such methods can perform risk analysis for specific SEs, they often fail to account for the coupling effects among multiple factors and SEs. Consequently, their adaptability to complex production environments remains limited. Moreover, such methods are often constrained to specific scenarios or event types, which hinders the effective prevention and control of key influencing factors. To overcome these limitations, it is necessary to fully leverage data-driven analytical approaches for comprehensive and systematic data integration and analysis. To this end, deepening the understanding of the coupling relationships between factors and utilizing these interconnections to construct an effective risk analysis model is important. Such a model is crucial for automatically optimizing factors and for identifying and assessing SEs.

In summary, data have become an effective means to uncover the underlying mechanisms of SEs and are increasingly demonstrating their core value in SE modeling. This study proposes an integrated risk analysis model combining theoretical analysis and data-driven approaches for SEs. The model establishes a mechanism for the cross-scale interactions between environmental factors and SEs. Focusing on cross-scale interactions, an environmental factor correlation representation model is proposed, which establishes measurable environmental factors (MEFs) that are related to SEs. The dynamic evolution trends of SEs over time are driven by the coupled interactions of various environmental factors. Based on the above theory, a data-driven model for identifying and assessing the risks of multiple types of SEs is established. This results in a new SE analysis model characterized by causative tracing, factor prioritization, and comprehensive warning. Finally, considering the complexity, dynamics, and frequent accident characteristics of coal mine production systems, this paper uses a coal mine production environment as a case study to analyze and validate the proposed model, offering practical solutions for addressing SEs in production environments.

## Literature review

Research on risk identification and assessment for multitype SEs under the coupling of environmental factors mainly encompasses two aspects: theoretical modeling and risk evaluation.

### The theory of SE causation

The theory of SE causation aims to establish the causal logic between internal factors and events, providing a theoretical support for understanding their evolutionary mechanisms<sup>15</sup>. Existing research has gradually developed an evolutionary trajectory from structured causal models to dynamic nonlinear models.

Early studies mainly adopted a structured causal modeling framework. These studies demonstrated that in production operations, the failure or sequential activation of protective mechanisms and causal chains under specific conditions can ultimately lead to the occurrence of SEs. Recent reliability studies further indicate that protective mechanisms may be conditionally triggered by multiple interacting factors, leading to diverse system outcomes under disturbances<sup>16</sup>. For example, the domino theory<sup>17</sup> indicates that accidents result from a chain reaction of causally linked events. The Swiss cheese model<sup>18,19</sup> posits that accidents occur due to the cumulative effects of latent hazards and active conditions across multiple layers of defense, intersecting in both time and space. Trajectory intersection theory<sup>20</sup> states that accidents arise from the coupling of unsafe human behaviors and unsafe object conditions within a shared spatiotemporal context. Epidemiological theory<sup>21</sup> reveals that accidents result from the interplay between human, environmental, and mediating factors. The system-theoretic accident model and processes<sup>22,23</sup> posits that accidents occur due to the inadequacy of control at various system levels, leading to ineffective regulation of the interactions between components. The 2–4 Model divides the causation of SEs into two levels and four stages, revealing the hierarchical relationships between direct and indirect causes<sup>24</sup>. These theories provide a clear structural framework for understanding the causal mechanisms underlying SEs. However, their reliance on qualitative reasoning and static analysis limits their ability to capture the dynamic evolution and nonlinear coupling among multiple factors in complex production systems. Existing studies further suggest that multi-factor dependencies may trigger cross-scale risk transfer, leading to cascading evolution patterns of SEs<sup>25,26</sup>.

Complex system and dynamic instability models focus on the transition of a system from a stable state to an unstable state under disturbances, revealing the time-varying and abrupt characteristics of SEs. Johnson developed the Change–Failure model, which posits that SEs originate from energy release and control failure<sup>27</sup>. The Functional Resonance Analysis Method (FRAM) conceptualizes SEs as emergent phenomena arising from nonlinear coupling and resonance among multiple functional modules within a system<sup>28</sup>. When the interactive effects among these functions exceed a critical threshold, the system transitions abruptly from a stable to an unstable state. Catastrophe theory<sup>29</sup> conceptualizes the occurrence of SEs as abrupt phase transitions of factor states in the vicinity of critical points. Collectively, these theories elucidate the nonlinear and emergent characteristics of SEs, providing an essential theoretical framework for interpreting the dynamic shift of production systems from safety to instability.

In summary, the theory of SE causation has evolved from structured causal mechanisms toward nonlinear coupling mechanisms, and from static structural descriptions to dynamic system modeling. Despite these advances, existing studies still exhibit notable limitations: (1) most theoretical approaches remain primarily qualitative, making it difficult to derive computable mappings from high-dimensional sensor data; and (2) quantitative characterization and causal attribution of multi-factor coupling are inadequate, limiting deeper insights into its influence on SE occurrence.

### Risk analysis models for SEs

Risk analysis methods are used to assess, identify and quantify the probability of SE occurrence. Existing studies can be broadly categorized into two types: event-chain analysis methods and factor-driven approaches.

Risk analysis method based on the event-chain perspective focuses on modeling the interrelationships between events. This type of approach aims to identify the root causes of critical events and calculate the associated risk probabilities. Feng et al.<sup>12</sup> developed a dynamic risk analysis framework for industrial systems based on an event-chain model, which reveals the evolutionary process of SEs across different stages. Li et al.<sup>30</sup> constructed a causal path network using complex network theory to quantify the influence weights among nodes, thereby achieving risk modeling of railway transportation systems. Li et al.<sup>31</sup> combined the fuzzy analytic hierarchy process and Bayesian network methodologies to develop a Bayesian network model for assessing gas explosion risks in coal mines. Zhang et al.<sup>32</sup> proposed a fuzzy Bayesian network-based safety risk analysis method for road construction scenarios, which achieves full life cycle risk management through causal analysis, fuzzy reasoning and sensitivity analysis. Feng et al.<sup>33</sup> proposed an event-chain-based dynamic risk analysis method that facilitates the assessment of causal importance and the formulation of optimal risk reduction strategies.

Risk analysis methods from the factor-driven perspective assess risks by capturing and quantifying the complex nonlinear relationships between factor states and SE occurrence probabilities. By monitoring and estimating the fluctuation trends of the hazard factors associated with SEs, potential hazards can be identified, and multilevel early warnings can be issued. Muduli et al.<sup>13</sup> employed fuzzy logic reasoning to assess spontaneous combustion risks in coal mines in real time by setting fuzzy sensor thresholds. Zhang et al.<sup>34</sup> proposed an adaptive warning method based on trend monitoring. Wang et al.<sup>35</sup> analyzed the variation patterns exhibited by electromagnetic radiation during coal and gas outburst processes, establishing an early warning model based on these signals. However, these methods are often affected by the complex coupling of factors and the ambiguity of critical conditions. To address this issue, scholars have introduced advanced methods such as machine learning and deep learning to implement more accurate risk assessments. Wang et al.<sup>36</sup> utilized big data technology to collect dynamic disaster parameters in mining areas and employed the adaptive boosting (AdaBoost) classification algorithm to predict rock burst risks. Li et al.<sup>37</sup> proposed a multisource information fusion warning model based on autoregressive integrated moving average and the transferable belief model, enabling real-time dynamic warnings for gas outburst risks in coal mines. Guo et al.<sup>38</sup> introduced a hybrid approach combining building information modeling and D-S evidence theory to integrate, assess, and visualize risk factors in underground tunnels. Shen et al.<sup>39</sup> proposed a cloud model-based risk assessment method for excavation and construction projects that estimates risk statuses through multisource data collection, model construction, and risk level determination.

Recently, extensive research has been conducted in the field of risk assessment. However, the following problems still exist. (1) Each SE is modeled independently, leading to a large workload and poor model compatibility. (2) Most methods focus on analyzing single SE with limited factors. The accuracy of the obtained results is significantly affected by the selection and comprehensiveness of these factors. (3) Such models fail to adequately consider the interrelationships between various factors and SEs. A unified analytical framework and an effective integration mechanism for systematically incorporating and comparing different types of risk information are lacking.

To address the limitations of the above research, this study makes the following contributions.

1. This paper establishes a cross-scale mechanism governing the effects of environmental factors on SEs. SEs are viewed as the results of multiple environmental factors interacting at the factor scale, which in turn produce cross-scale emergent effects at the event scale.
2. At the factor scale, an environmental factor correlation model is established, and the MEFs related to SEs are determined. At the event scale, a chain mechanism depicting the transformation and superposition of multiple types of SEs is elucidated. Regarding cross-scale dynamics, the cross-scale emergence mechanism concerning the effects of environmental factors on SEs is analyzed, with an emphasis on tracing the differential contributions of these factors.
3. Based on the proposed theoretical model, a data-driven risk identification and assessment model is constructed for multitype SEs under the coupling of environmental factors. The interpretability of the model enables the quantification of the relevance levels and contributions of environmental factors.

## Theoretical foundation

### Definitions of SEs and environmental factors

Events, as defined temporal and spatial occurrences, encompass both positive and negative aspects<sup>40</sup>. SEs represent a subset of such events, denoting events that have adverse impacts on a production system. Environmental factors are pivotal elements for understanding, identifying, and analyzing the occurrence of SEs. Therefore, SEs and environmental factors belong to different scales with different portrayals and descriptions. Environmental factors include those that characterize, quantify, and explain SEs. SEs arise as emergent properties from the nonlinear interactions of various environmental factors.

Figure 1 shows the cross-scale relationships between SEs and environmental factors. At the event scale, SEs interact, constituting a directed chain network structure. As a special subset of the SE set, accidents gradually evolve from related SEs. At the factor scale, the environmental factors exhibit a certain degree of hierarchical dynamic correlation. State information is deeply integrated among the related environmental factors. A constellation of environmental factors determines the cross-scale emergence of SEs. Under specific spatiotemporal conditions, the state changes exhibited by these factors interact through nonlinear dynamics, resulting in emergent outcomes. In general, the state changes undergone by environmental factors generate an intrinsic motivation for the dynamic evolution of SEs. The dynamic evolution of an SE is the macroscopic manifestation of the state changes of environmental factors. The mathematical representation of the relationship between SEs and environmental factors is shown in Eq. (1).

$$s_1, s_2, \dots, s_o = \mathcal{F}(a_1, a_2, \dots, a_f) \tag{1}$$

where  $\mathcal{F}$  is the emergence function concerning the effect of environmental factors on SEs,  $a_i$  is an environmental factor,  $\mathbb{A} = \{a_1, a_2, \dots, a_f\}$  is a set of environmental factors,  $s_j$  is an SE, and  $\mathbb{S} = \{s_1, s_2, \dots, s_m\}$  is a set of SEs.

The definitions of SEs and environmental factors are improved and supplemented.

**Definition 1** Environmental factors refer to factors within a production environment that are actively influenced by production activities, and status changes can directly affect the production environment, potentially leading to SEs.

**Definition 2** SEs refer to emergent outcomes that arise within a specific temporal and spatial context due to state changes exhibited by the environmental factors within a production environment, potentially having adverse impacts on the production system.

Taking gas explosion in coal mines as an example, the hierarchical linkage from environmental factors to safety events is formally illustrated to clarify the cross-scale emergence mechanism.

Let gas concentration, oxygen concentration, and temperature be denoted as  $a_1, a_2, a_3$  respectively. These variables belong to the set of environmental factors,  $a_1, a_2, a_3 \in \mathbb{A}$ .

Let the environmental factor states at time  $t$  be  $X^t(a_1), X^t(a_2), X^t(a_3)$ . For each factor, an instability domain is defined as  $\Omega_1, \Omega_2, \Omega_3$ , respectively. When the factor state reaches or exceeds its instability domain, the corresponding precursor safety event is triggered. Specifically, the precursor events are defined as:  $s_{p1} = \{t : X^t(a_1) \in \Omega_1\}$ ,  $s_{p2} = \{t : X^t(a_2) \in \Omega_2\}$ ,  $s_{p3} = \{t : X^t(a_3) \in \Omega_3\}$ , with indicator functions  $1_{s_{p1}} = 1 \{X^t(a_1) \in \Omega_1\}$ ,  $1_{s_{p2}} = 1 \{X^t(a_2) \in \Omega_2\}$ ,  $1_{s_{p3}} = 1 \{X^t(a_3) \in \Omega_3\}$ . Such conditions typically indicate high risk, although they may not yet correspond to an actual accident outcome. They therefore fall within the scope of early-warning safety events.

Gas concentration exceedance, sufficient oxygen availability, and abnormal temperature rise represent critical transitions of environmental factors beyond their stability boundaries, leading to a significant degradation of system safety. Let the emergent terminal safety event “gas explosion” be denoted as  $s_1$ , where  $s_1 \in \mathbb{S}$ . The occurrence of gas explosion is driven by the coupled effects of the three key environmental factors and can be expressed as a cross-scale emergence result, i.e.,  $s_1 = s_{p1} \cap s_{p2} \cap s_{p3}$ ,  $1_{s_1} = 1_{s_{p1}} \cdot 1_{s_{p2}} \cdot 1_{s_{p3}}$ .

This example illustrates that factor-level instability states can interact and chain together, thereby giving rise to an emergent event at the event scale. Explicitly distinguishing factor-level instabilities and event-level outcomes provides a clearer basis for mechanism interpretation and quantitative risk assessment.

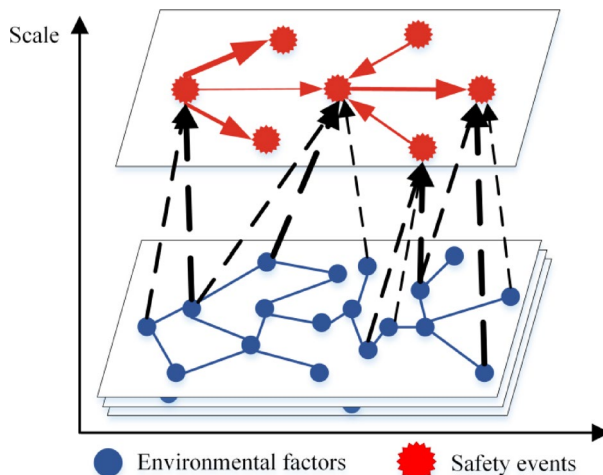


**Fig. 1.** The cross-scale relationships between SEs and environmental factors.

## The scale characteristics of SEs and environmental factors

### *The correlations of environmental factors*

In production systems, environmental factors do not exist in isolation from each other but rather in a situation involving interdependence, influence and constraint. It is difficult to clarify the correlations among all environmental factors. Instead, breaking down the complex issue of environmental factors influencing an entire system into localized issues that are associated with specific SEs can serve as an effective strategy. By focusing on SEs, specialized models can be developed to deepen the understanding of the dynamic correlations among various environmental factors. Furthermore, this approach provides a structured and progressive method for enhancing the comprehension of complex systems. Notably, relevance refers to the interdependence between environmental factors. This dependence shows that a change in one environmental factor state may lead to a change in another environmental factor state, and vice versa, exhibiting a two-way characteristic.

Generally, only a few critical environmental factors play decisive roles in the occurrence of SEs. Other environmental factors, though not directly causative, are intricately linked to these core factors, indirectly influencing SEs. For instance, gas outburst events are directly affected by the interplay among the coal structure, ground stress, and gas occurrence of coal seam<sup>41</sup>. Additionally, factors such as coal rigidity and drilling cutting weight also play a role in gas outbursts, albeit indirectly. These factors typically quantify and reflect the critical core factors. For instance, coal rigidity represents the physical and mechanical properties of coal structure, while drilling cutting weight indicates ground stress levels<sup>42</sup>. Therefore, the correlation mapping relationships of environmental factors can be subdivided by taking SEs as the research objects, the occurrence mechanism as guidance, and relevant research as the basis. On this basis, disaster-causing environmental factors, derived environmental factors, and measurable environmental factors (MEFs) are established. Their definitions are as follows.

**Definition 3** Disaster-causing environmental factors refer to the critical environmental elements that significantly affect and jointly contribute to shaping the occurrence, evolution, and spread patterns of SEs under specific conditions.

**Definition 4** Derived environmental factors refer to subenvironmental elements that act as indicators for characterizing disaster-causing environmental factors, the states of which are difficult to obtain directly without specific technical support.

**Definition 5** MEFs refer to those that can be quantitatively assessed and from which data or information can be directly captured using current technological means.

Let the set of disaster-causing environmental factors be  $\mathbb{D}$ , the set of derived environmental factors be  $\mathbb{H}$ , and the set of MEFs be  $\mathbb{V}$ , where  $\mathbb{A} = \{\mathbb{D}, \mathbb{H}, \mathbb{V}\}$ . Disaster-causing environmental factors play a fundamental and guiding role in mining derived environmental factors and MEFs. Due to the production environment and technology limitations, it is difficult to determine the states of some disaster-causing environmental factors. In this case, the derived environmental factors transmit and transform the state information of the disaster-causing environmental factors and MEFs. The MEFs provide reliable data for the study of SEs. Notably, the derived environmental factors and MEFs can be transformed into each other under the influence of different environmental and technical conditions. For example, when the production environment is equipped with sensors for specific derivative environmental factors, these derivative environmental factors can be measured and converted into measurable factors. In contrast, if no corresponding support can be provided by sensing technology, the derived environmental factors cannot be directly quantified and thus maintain their unmeasurable state. With the advancement of measurement technology and the application of sensors, derivative environmental factors that were originally difficult to measure directly will gradually be included in the measurable category. The relationships among the three types of feature are  $\mathbb{D} \cap \mathbb{H} = \emptyset$ ,  $\mathbb{H} \cap \mathbb{V} = \emptyset$ , and  $\mathbb{D} \cap \mathbb{V} \neq \emptyset$ , as shown in Fig. 2

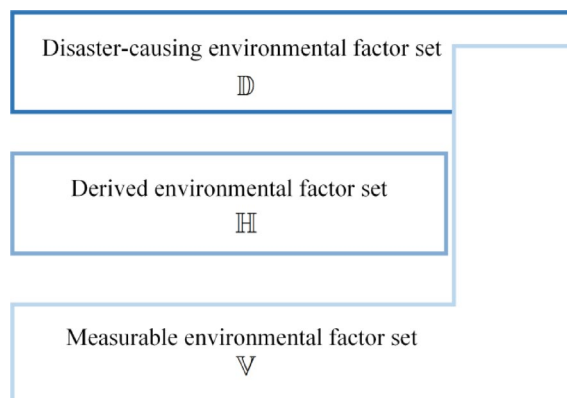


**Fig. 2.** Relationships between sets of environmental factors.

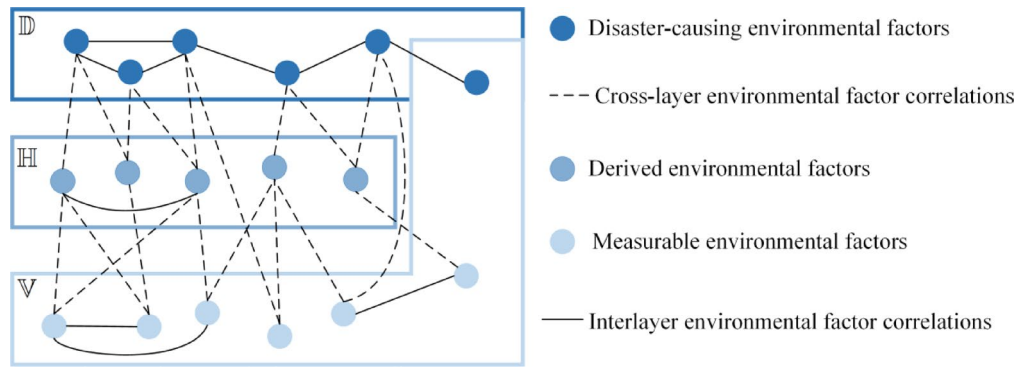


**Fig. 3.** Hierarchical correlations of environmental factors.

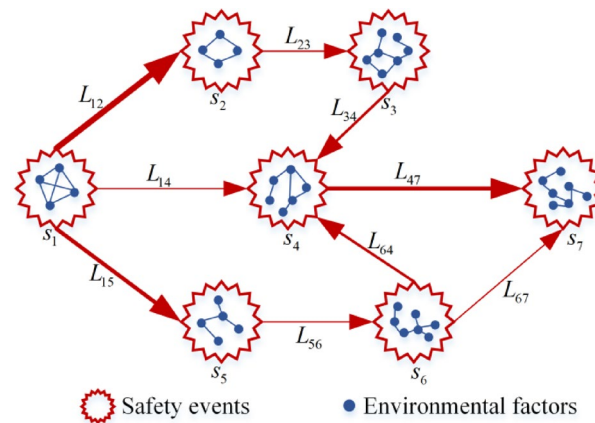


**Fig. 4.** The chain relationships of SEs.

Figure 3 illustrates the hierarchical associations of environmental factors, showing their bidirectional interactions. Environmental factors are connected both across different levels and within the same level. When the state of an environmental factor changes, this change can gradually influence the related environmental factors through their connections. As a result, the related environmental factors receive change information and update their states accordingly. The equation for the state transfer and aggregation process applied to associated environmental factors are shown in Eq. (2).

$$g_i^{t+1} = \sum \mathcal{G}(X^t(v_i), X^t(e(v_i))) \tag{2}$$

where  $\mathcal{G}$  is the state transfer and aggregation function,  $v_i$  is an MEF,  $g_i^{t+1}$  is the state change information received by  $v_i$  at time  $t + 1$ ,  $X^t(v_i)$  is the state of  $v_i$  at time  $t$ ,  $e(v_i)$  is the factor associated with  $v_i$ , and  $X^t(e(v_i))$  is the state of the environmental factor associated with  $v_i$  at time  $t$ .

The state change information received at time  $t + 1$  is brought into Eq. (3) to update the state  $v_i$  at time  $t + 1$ :

$$X_i^{t+1}(v_i) = \mathcal{H}(X_i^t(v_i), g_i^{t+1}) \tag{3}$$

where  $\mathcal{H}$  is the state update function and  $X_i^{t+1}(v_i)$  is the state of  $v_i$  at time  $t + 1$ .

Based on the state transmission and update mechanism obeyed by associated environmental factors, it can be inferred that MEFs are fundamental for gathering complete state data related to the associated environmental factors. Therefore, the states of MEFs can represent the state information of disaster-causing environmental factors, thereby providing reliable data inputs for SE studies.

*Chain modeling between SEs*

The chain relationships of SEs consists of a directed complex network formed by multiple SEs and their evolutionary pathways. Within production systems, the occurrence of SEs is influenced by the state changes exhibited by various environmental factors, as depicted in Fig. 4. As these environmental factors approach and fall within the instability domain, the corresponding production system becomes inherently unstable, leading to the dynamic spread and propagation of SEs. The nature of this propagation further poses a substantial threat to the operational safety and stability of production systems.

The link strengths between different SEs vary significantly, resulting in varied degrees of interconnection and diverse probabilities of neighboring SEs being triggered. Therefore, the occurrence of SEs is influenced not only by their inherent probabilities but also by the interconnections within the network of neighboring SEs, as depicted in Eq. (4).

$$P(s_j) = \mathcal{P}(P_0(s_j), P(e(s_j)), L(e(s_j) \rightarrow s_j)) \tag{4}$$

where  $P_0(s_j)$  is the intrinsic probability of an SE  $s_j$ ,  $P(s_j)$  is the occurrence probability of  $s_j$ ,  $e(s_j)$  is the neighbor SE of  $s_j$ ,  $P(e(s_j))$  is the occurrence probability of the neighbor SE,  $L$  is the link strength of the neighbor SE triggering  $s_j$ , and  $\mathcal{P}$  is the probabilistic function for predicting the occurrence of the SE.

In addition, shared environmental factors often underlie diverse SEs. Comprehensively analyzing multiple types of SEs can be valuable for facilitating the identification of SEs, as well as for identifying and controlling the critical environmental factors.

*The cross-scale interactions between environmental factors and SEs*

Figure 5 illustrates the cross-scale interactions between environmental factors and SEs. At the factor scale, environmental factors exhibit a high degree of interconnectivity, resulting in the dynamic transmission and continuous updating of state information. At the event scale, SEs rarely occur in isolation; instead, they often propagate in a sequential or cascading manner. Through cross-scale interactions and influences, dynamic nonlinear couplings among environmental factors accumulate and ultimately manifest in the occurrence of SEs. When an SE occurs, the states of the environmental factors often exhibit fluctuating upward or downward trends. However, the contributions of various environmental factors to SEs differ significantly. The variability in their contributions reflects the relative importance of different environmental factors to SEs and influences the accuracy of the output analysis results. Therefore, accurately capturing the dynamic state changes exhibited by environmental factors lays the cornerstone for elucidating the intricate cross-scale emergence processes of SEs. The degree of contribution is key to measuring the extent to which each environmental factor influences the occurrence of SEs.

For the set of SEs  $\mathbb{S}$ , the corresponding set of disaster-causing environmental factors is  $\mathbb{D}$ . A function representing the cross-scale impact of disaster-causing environmental factors on SEs is established, as shown in Eq. (5).

$$\mathbf{P} = \mathcal{P} \left( \mathcal{S} \left( \boldsymbol{\beta} \sum_{i=1}^m X(d_i) \right) \right) \tag{5}$$

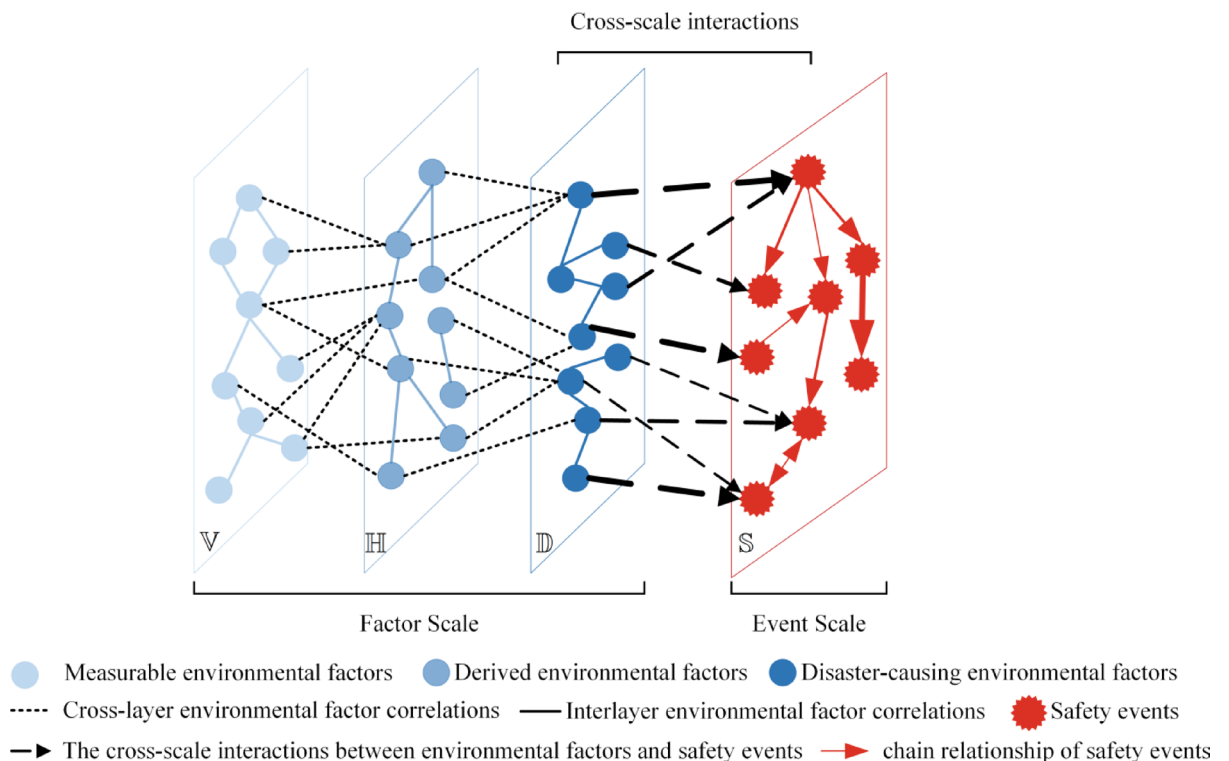


**Fig. 5.** The cross-scale interactions between environmental factors and SEs.

where  $d_i$  is a disaster-causing environmental factor,  $X(d_i)$  is the state of  $d_i$ ,  $S$  is the cross-scale interaction function,  $\beta$  is the contribution matrix, and  $\mathbf{P}$  is the probability matrix for the occurrence of an SE.

Due to production environment and technical condition limitations, obtaining the state change information of some disaster-causing environmental factors is difficult. Based on Eqs. (2)-(3), it can be inferred that MEFs can significantly reflect the state change information of disaster-causing environmental factors. Thus, MEFs can serve as a crucial data foundation for SE analyses. Moreover, constructing an inference mechanism for MEFs with respect to SEs also aids in analyzing SEs.

Figure 6 establishes the reasoning architecture of the MEFs for SEs. Let the set of MEFs be  $\mathbb{V} = \{v_1, v_2, v_3, \dots, v_f\}$  and the states of the MEFs be  $\mathcal{X} = [\mathbf{X}(v_1), \mathbf{X}(v_2), \mathbf{X}(v_3), \dots, \mathbf{X}(v_f)]$ . A mapping function from MEFs to SEs is established as  $q : \mathcal{X} \rightarrow 2^{\mathbb{S}}$ . First, we capture the key information contained in the MEF data. Based on the data structures of  $\mathbb{S}$  and  $\mathcal{X}$ , a specific function  $\mathbf{C} = \mathcal{C}(\mathbf{X}(v_i), \mathbf{X}(v_j) | \mathbb{S})$  is constructed to capture the correlations among the MEFs. On this basis, we utilize the formula  $\mathbf{I} = \mathcal{K}(\mathbf{C}, \mathcal{X})$  to highlight the key information contained in the data. Second, the cross-scale mapping driven by the contributions of the MEFs to SEs is analyzed. A dimensionality reduction projection function  $\mathbf{EI} = \mathcal{L}(\beta, \mathbf{I}, \mathbb{S})$  is established to map  $\mathbf{I}$  to the SEs. Here,  $\mathbf{EI}$  denotes the effective information extracted from  $\mathbf{I}$  to the SEs. Subsequently, the SEs are identified and assessed. The occurrence probability of the SEs is  $\mathbf{P} = \mathcal{P}(\mathbf{EI})$ . Finally, in the SE feedback and optimization phase, the parameters and weights of the inference process are adjusted and optimized through gradient reversal. This series of inference steps aids in the optimal selection and adaptive matching of the MEFs, as well as the accurate identification of the SEs.

### Risk identification and assessment model for multitype SEs

#### Problem description

Let  $\mathbb{V} = \{v_1, v_2, v_3, \dots, v_f\}$  be a set of MEFs and  $\mathbb{S} = \{s_1, s_2, \dots, s_m\}$  be a set of SEs. The SE identification and assessment task involves learning a function denoted as  $q : \mathcal{X} \rightarrow 2^{\mathbb{S}}$  from the training set  $\{(\mathcal{X}_i, \mathcal{Y}_i) | 1 \leq i \leq n_{\text{samples}}\}$ , which contains  $n_{\text{samples}}$  samples. For each sample  $(\mathcal{X}_i, \mathcal{Y}_i)$ ,  $\mathcal{X}_i = [X_i(v_1), X_i(v_2), \dots, X_i(v_f)] \in \mathbb{R}^f$  represents the  $f$ -dimensional MEF input. Furthermore,  $\mathcal{Y}_i = [Y_i(s_1), Y_i(s_2), \dots, Y_i(s_m)] \in \mathbb{R}^m$  represents states of multitype SEs associated with  $\mathcal{X}_i$ , which is encoded as a binary vector. If there exists an  $\mathcal{X}_i$  that leads to the occurrence of an SE  $s_j$ ,  $Y_i(s_j)$  is 1; otherwise, it is 0. Let  $\{\mathcal{X}_p | 1 \leq p \leq n_{\text{unlearned}}\}$  denote the dataset of MEFs for which the corresponding SEs are unknown. This study aims to learn the function  $q : \mathcal{X} \rightarrow 2^{\mathbb{S}}$  that predicts the set of potential SEs  $\mathcal{Y}_p \subseteq \mathbb{S}$  to minimize the induced predictive error. The overall formulation and dataset definition for the SE identification and assessment task are summarized in Table 1. All notations and definitions are provided in the Supplementary Material (Table A1).

$$\theta^* = \arg \min_{\theta} \left[ \frac{1}{m} \sum_1^m L(q(\mathcal{X}_p; \theta), \mathcal{Y}_p) \right] \tag{6}$$

where  $L(\cdot)$  is the loss function and  $\theta^*$  and  $\theta$  are model parameters.

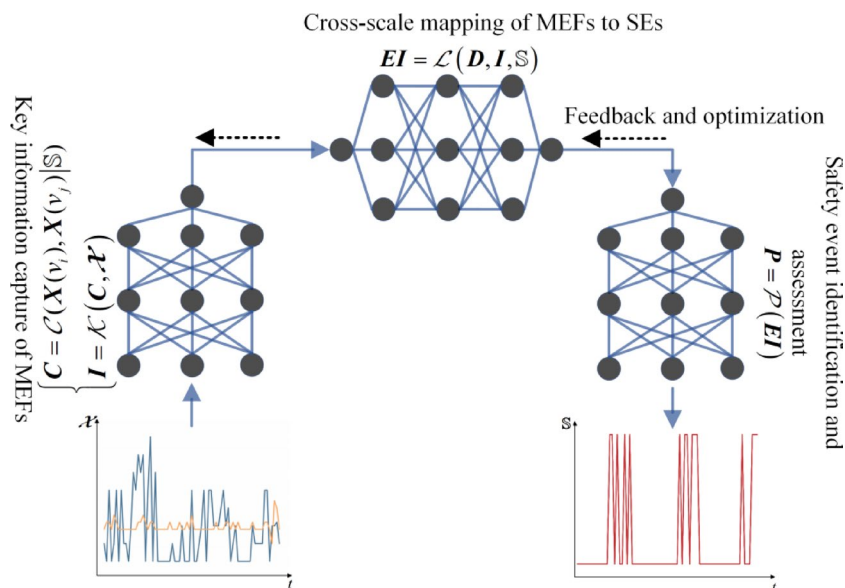
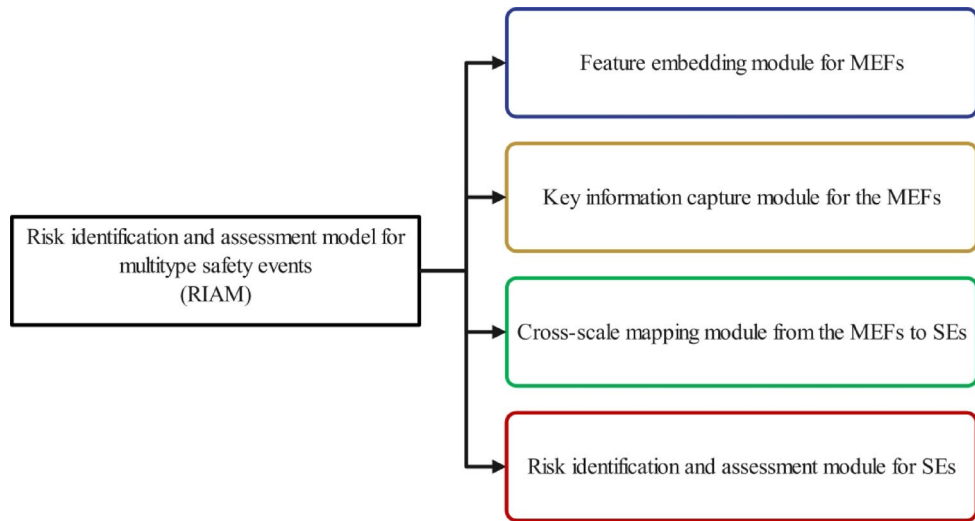


Fig. 6. The reasoning architecture for mapping MEFs to SEs.

$\mathcal{X}_t$					$Y(s_1)$	$Y(s_2)$	...	$Y(s_m)$
1	$X_1(v_1)$	$X_1(v_2)$	...	$X_1(v_f)$	0	1	...	1
2	$X_2(v_1)$	$X_2(v_2)$	...	$X_2(v_f)$	0	0	...	1
...	...	...	...	...	...	...	...	...

**Table 1.** Datasheet for SE identification and assessment tasks.



**Fig. 7.** Module composition of the multitype SE risk identification and assessment model.

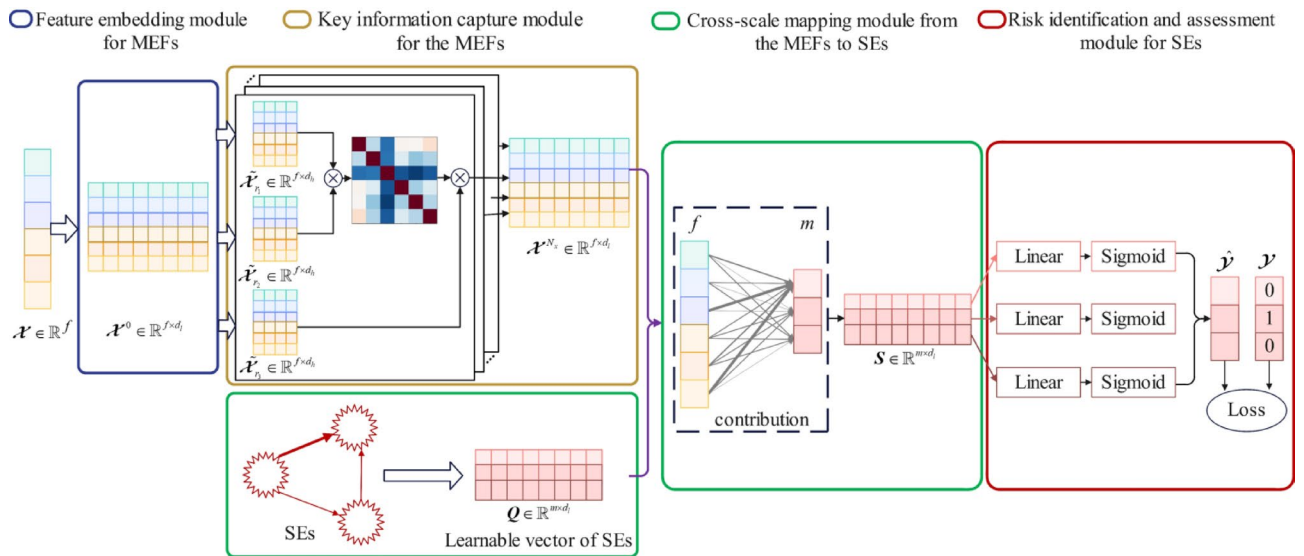


**Fig. 8.** The general framework of the RIAM.

**Overall framework**

The multitype SE risk identification and assessment model (RIAM) consists of four main modules, i.e., a feature embedding module for MEFs, a key information capture module for the MEFs, a cross-scale mapping module from the MEFs to SEs, and a risk identification and assessment module for the SEs, as shown in Fig. 7. Figure 8 illustrates the general framework of the model.

*Feature embedding module for MEFs*

The MEFs originate from multiple sources with diverse units, resulting in scale inconsistency if directly used as model inputs. Therefore, the MEF state vector  $\mathcal{X} \in \mathbb{R}^f$  is normalized feature-wise to remove unit-dependent

scale differences. Let  $\mathcal{X} = [X_1, X_2, \dots, X_f] \in \mathbb{R}^f$ . Each feature is standardized by z-score normalization:  $\tilde{X}_j = \frac{X_j - \mu_j}{\sigma_j}$ , yielding  $\tilde{\mathcal{X}} = [\tilde{X}_1, \tilde{X}_2, \dots, \tilde{X}_f] \in \mathbb{R}^f$ . Where  $\mu_j$  and  $\sigma_j$  are computed from the training set only and then applied to the validation/test sets to avoid information leakage.

After preprocessing normalization, a feature embedding module is designed to achieve a unified representation and effective feature extraction from heterogeneous inputs. Specifically, it applies linear transformation and Layer Normalization (LN) to project the normalized MEF vector into a unified latent space of dimension  $d$ .

$$\mathcal{X}^0 = LN(\mathbf{W}_h \tilde{\mathcal{X}} + \mathbf{b}_h) \tag{7}$$

where  $\mathbf{W}_h \in \mathbb{R}^{f \times d_l}$  and  $\mathbf{b}_h \in \mathbb{R}^{f \times d_l}$  denote the feature embedding matrix and bias term, respectively.  $LN(\cdot)$  denotes the Layer Normalization operation, and the output  $\mathcal{X}^0 \in \mathbb{R}^{f \times d_l}$  represents the feature embedding of each MEF in the  $d$ -dimensional latent space.

*Key information capture module for the MEFs*

The key information capture module is designed to model latent couplings among MEFs. It employs an adaptive mechanism to capture inter-factor dependencies and nonlinear interactions, thereby enabling the dynamic representation of critical risk information. It comprises  $N_x$  stacked layers, each involving correlation-weight learning and representation update, followed by residual and Layer Normalization refinements.

Taking the MEF representation vector  $\mathcal{X}^{k-1} (k = 1, 2, \dots, N_x)$  as input, it is divided into  $u$  parallel processing units. Each unit performs a linear transformation to learn inter-factor correlations and adaptively update the representations:

$$\begin{cases} \mathbf{U}^n = \text{soft max} \left( \frac{\tilde{\mathcal{X}}_{r_1} \cdot \tilde{\mathcal{X}}_{r_2}^T}{\sqrt{d_h}} \right) \tilde{\mathcal{X}}_{r_3} \\ \tilde{\mathcal{X}}^{k,(1)} = \text{concat}(\mathbf{U}^1, \mathbf{U}^2, \dots, \mathbf{U}^u) \mathbf{W}^O \\ \tilde{\mathcal{X}}^k = LN(\mathcal{X}^{k-1} + \tilde{\mathcal{X}}^{k,(1)}) \end{cases} \tag{8}$$

where  $\mathbf{U}^n (n = 1, 2, \dots, u)$  denotes the output of the  $n$ -th processing unit,  $\tilde{\mathcal{X}}_{r_1}, \tilde{\mathcal{X}}_{r_2}, \tilde{\mathcal{X}}_{r_3} \in \mathbb{R}^{f \times d_h} (d_h = d_l/u)$  represents the linearly transformed representation of the input  $\mathcal{X}^{k-1}$ ,  $\text{concat}(\cdot)$  denotes the concatenation of the results of each processing unit, and  $\mathbf{W}^O \in \mathbb{R}^{d_l \times d_l}$  is a learnable parameter matrix.

To better extract salient patterns and capture complex inter-factor dependencies, a nonlinear transformation is applied, formulated as:

$$\mathcal{X}^{k,(2)} = \text{Gelu}(\tilde{\mathcal{X}}^k \mathbf{W}_{r_4} + \mathbf{b}_{r_4}) \mathbf{W}_{r_5} + \mathbf{b}_{r_5} \tag{9}$$

$$\mathcal{X}^k = LN(\mathcal{X}^{k,(2)} + \tilde{\mathcal{X}}^k) \tag{10}$$

where  $\text{Gelu}(\cdot)$  is the activation function,  $\mathbf{W}_{r_4}$  and  $\mathbf{W}_{r_5}$  are the weight matrices and  $\mathbf{b}_{r_4}$  and  $\mathbf{b}_{r_5}$  are the deviations of the linear transformation, and  $\mathcal{X}^{k-1}, \mathcal{X}^k \in \mathbb{R}^{f \times d_l} (k = 1, 2, \dots, N_x)$  denote the outputs of the  $(k-1)$ -th and  $k$ -th layers of the key information capture module.

*Cross-scale mapping module from the MEFs to SEs*

Different safety events rely on different subsets of environmental factors. To capture such event-specific dependencies, a cross-scale mapping module is developed to quantify the contribution of each measurable factor to each event and to map environmental states into event-specific risk representations. For each SE, a learnable vector  $\mathbf{Q} \in \mathbb{R}^{m \times d_l}$  is defined. By constructing weighted interactions between MEFs and SEs, the module establishes a cross-scale mapping that performs directional aggregation of environmental information toward each event:

$$\begin{cases} \beta = \text{soft max} \left( \frac{\mathbf{Q} \cdot (\mathcal{X}^{N_x})^T}{\sqrt{d_l}} \right) \\ \mathbf{S} = \beta \mathcal{X}^{N_x} \end{cases} \tag{11}$$

where  $\beta \in \mathbb{R}^{m \times f}$  denotes the contribution-weight distribution of MEFs to SEs,  $\mathcal{X}^{N_x}$  is the  $N_x$ -th layer output of the key information capture module, and  $\mathbf{S} \in \mathbb{R}^{m \times d_l}$  represents the aggregated feature vector of SEs obtained from all environmental-state information.

*Risk identification and assessment module for SEs*

For multi-type SE discrimination, the module employs independent classification heads for each event type with parallel outputs, allowing the model to learn event-specific discriminative features in distinct subspaces.

For each event:

$$\begin{aligned} \hat{\mathbf{P}}_j &= \mathbf{W}_j \mathbf{S}_j + \mathbf{b}_j, j = 1, 2, \dots, m \\ \mathbf{P}_j &= \text{Sigmoid}(\hat{\mathbf{P}}_j) \end{aligned} \tag{12}$$

The overall output for multi-type safety events can be expressed as:  $\mathbf{P} = [\mathbf{P}_1, \mathbf{P}_2, \dots, \mathbf{P}_m]$ . A reference threshold  $\delta (0 \leq \delta \leq 1)$  yields the final decisions:

$$\hat{\mathbf{Y}}_{ij} = \begin{cases} 1 & \mathbf{P}_{ij} > \delta \\ 0 & \mathbf{P}_{ij} \leq \delta \end{cases} \quad (13)$$

where *sigmoid* is an activation function,  $\mathbf{P}_j$  is the predicted probability, and  $\hat{\mathbf{Y}}_{ij}$  is the risk identification and assessment result of an SE.

### Loss function

Given the concurrent and interdependent nature of safety events, the RIAM model employs the BCEWithLogitsLoss function to compute the multi-label prediction error and the Adam optimizer to update all trainable parameters during training.

$$L(\mathbf{P}, \mathcal{Y}) = -\frac{1}{n_{\text{samples}} \cdot m} [(\mathbf{W}_{pos} \odot \mathcal{Y}) \odot \log(\mathbf{P}) + (1 - \mathcal{Y}) \log(1 - \mathbf{P})] \rightarrow \min \quad (14)$$

where  $n_{\text{samples}}$  denotes the total number of samples,  $m$  represents the total number of safety event types, and  $\mathbf{W}_{pos} \in \mathbb{R}^m$  is the weight vector assigned to each safety event type.

### Case study

Coal and gas outburst is a typical high-disaster-risk scenario in deep coal mining operations. Its causation is complex and highly destructive, often triggered by the combined effects of multiple geological and environmental factors. In practical operations, several representative abnormal conditions—such as excessive initial gas velocity in boreholes and abnormal gas desorption indices—are often regarded as precursor signals of disaster events. Although these indicators do not constitute terminal events themselves, their over-threshold states usually indicate that the system is approaching an unstable and hazardous condition, thus possessing significant value for risk identification and intervention. When multiple factors simultaneously enter the instability domain, the overall risk level rises sharply, and an outburst may even be triggered. Therefore, simultaneously predicting both the occurrence of catastrophic events and their preceding high-risk states is of great significance for the comprehensive judgment capability of early warning systems.

To verify the performance and feasibility of the RIAM model in identifying different types of SEs under multi-factor coupling conditions, this section employs multi-type SEs as output variables. Early warning events are used to identify high-risk precursor signals, while the coal and gas outburst serves as the terminal SE. Through joint learning, potential risks can be identified and corresponding preventive measures can be implemented. Let  $s_1$  represents the coal and gas outburst,  $s_2$  denotes the initial velocity of borehole gas emission that exceeds the imposed limit, and  $s_3$  indicates the gas adsorption index of drilling cuttings exceeding the limit. The set of SEs to be studied is  $\mathbb{S} = \{s_1, s_2, s_3\}$ .

### Determination of MEFs

The model input consists of time-series data of MEFs obtained from coal mine production environments. The hypothesis of integrated action identifies the disaster-causing factors of coal and gas outbursts: coal structure, ground stress, and gas occurrence of coal seam. However, the ability to obtain data on these disaster-causing environmental factors is influenced by the production environment and technical limitations. Table 2 presents the correlation mappings of the environmental factors derived from established causal mechanisms, laboratory experiments, research studies, and field observations. The identified MEFs include the initial velocity of borehole gas emission ( $v_1$ ), drilling cutting weight ( $v_2$ ), gas adsorption index of drilling cuttings ( $v_3$ ), soft coal seam thickness ( $v_4$ ), EMR intensity ( $v_5$ ), and EMR pulses ( $v_6$ ).

### Data source

The dataset utilized in this study was collected from field measurements conducted at the Jiulishan Coal Mine, located in Henan Province, China<sup>45</sup>. Owing to the complex geological structure and dynamic gas environment, this mine provides a representative underground scenario for investigating the coupling effects of multiple environmental factors (MEFs) and the evolution of safety events (SEs) during tunneling operations. However, effective labeled samples are limited due to the sporadic and unpredictable nature of gas outburst-related events

MEF	Reflected disaster-causing environmental factors	References
$v_1$	coal structure, gas occurrence of coal seam	Tang et al. <sup>43</sup> ; Zhang et al. <sup>44</sup>
$v_2$	ground stress, coal structure	Li et al. <sup>45</sup> ; Wang et al. <sup>46</sup>
$v_3$	coal structure, gas occurrence of coal seam	Xue et al. <sup>47</sup> ; Wang et al. <sup>48</sup>
$v_4$	coal structure	Lama et al. <sup>49</sup> ; Zhai et al. <sup>50</sup>
$v_5$	coal structure, ground stress	Wang et al. <sup>51</sup> ; Qiu et al. <sup>52</sup>
$v_6$	coal structure, ground stress	Qiao et al. <sup>53</sup> ; Zhang et al. <sup>54</sup>

**Table 2.** The correlation mappings of environmental factors.

and their precursors, which may lead to insufficient coverage of rare conditions and increase the risk of model overfitting.

To address sample scarcity while maintaining the physical consistency of monitoring signals, a hybrid data augmentation strategy was adopted. The strategy consists of (i) perturbation-based augmentation to emulate sensor uncertainty and operational fluctuations, and (ii) conditional synthesis to expand feature-consistent samples under label constraints. Specifically, all raw features were first normalized into the range  $[0, 1]$  using Min–Max scaling. Then, Gaussian noise<sup>55</sup> injection was performed in the normalized feature space:

$$\bar{x} = x + \varepsilon, \varepsilon \sim \mathcal{N}(0, \sigma^2) \quad (15)$$

where  $\sigma$  was set to 0.03, and the perturbed values were clipped to  $[0, 1]$  to avoid invalid ranges. This perturbation strategy increases sample diversity while maintaining local continuity of MEFs, and improves model robustness to unavoidable sensor-level disturbances in underground environments.

To further capture nonlinear dependency structures among MEFs and enhance minority-condition coverage, a conditional generative adversarial network (CGAN) was employed for label-conditional synthesis. The generator maps latent noise  $z \sim \mathcal{N}(0, I)$  into synthetic feature vectors conditioned on binary labels (safety status vs. gas outburst), while the discriminator distinguishes real from synthetic samples under the same conditioning mechanism. The CGAN was trained using the Adam optimizer (learning rate 0.0002, betas = (0.5, 0.999)) for 100 epochs with batch size 32 and latent dimension  $d_z = 6$ . Synthetic samples were generated separately for each label to obtain a more balanced training distribution across the two classes.

Importantly, to strictly avoid data leakage, the entire augmentation process was conducted after cross-validation splitting and only within the training subset of each fold. That is, for each fold, the dataset was first split into training and validation subsets; augmentation was applied exclusively to the training subset, while the validation subset remained unchanged and was never used in CGAN training or sample generation.

Figure 9 compares the Kernel Density Estimation (KDE) distributions of six key precursor variables between the original and augmented datasets. Overall, the density curves exhibit a high degree of alignment in peak locations and distributional shapes, indicating that the augmentation process preserves the essential statistical characteristics of the measured monitoring data. Meanwhile, slight enrichment in low-frequency regions can be observed for some variables, suggesting that the introduced perturbations and CGAN-based synthesis provide additional sample diversity while remaining consistent with the underlying data manifold.

In addition, t-distributed stochastic neighbor embedding (t-SNE)<sup>56</sup> was employed to project the combined dataset into a low-dimensional space for visualization, where local neighborhood relations are approximately preserved. As shown in Fig. 10, augmented samples remain coherent with the original data manifold and maintain class-level separability, supporting that the generated samples are feature-consistent and label-conditional.

It should be emphasized that data augmentation in this work is introduced as a practical measure to improve training stability and robustness under sample scarcity.

### Performance metrics

In a SE risk assessment task, traditional methods for evaluating single SEs often rely heavily on accuracy. This metric is used as the primary evaluation criterion to gauge the precision of models in terms of accurately identifying specific SEs. However, this singular evaluation strategy is inadequate for the comprehensive risk identification and assessment of multiple types of SEs. This limitation becomes more pronounced under label imbalance, which is evident in our dataset: the positive rates of  $s_1$  and  $s_3$  are 20.55% and 19.18%, respectively, whereas  $s_2$  is an extremely rare label with only 6.85% positive samples. Under these conditions, accuracy

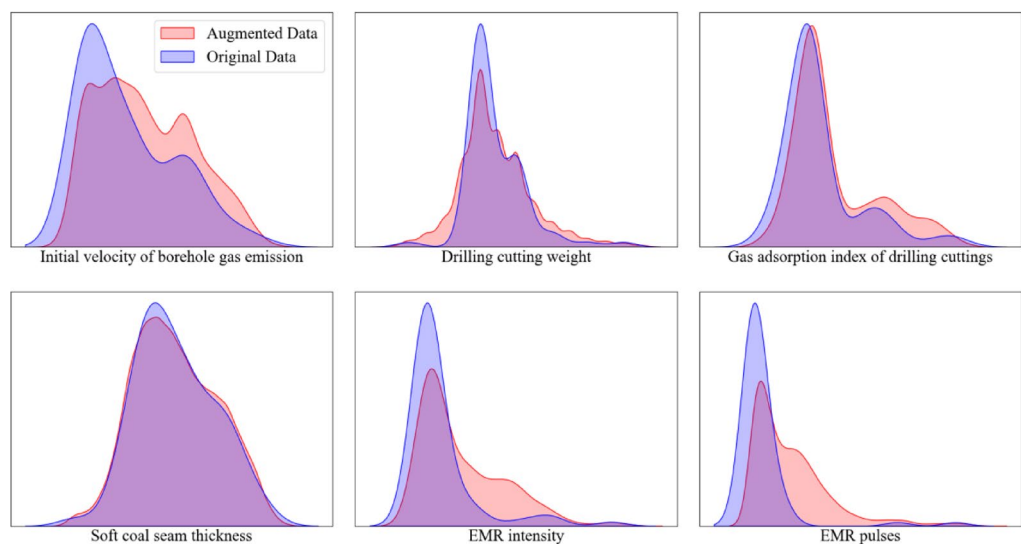


**Fig. 9.** Kernel density distributions of the augmented and original data.

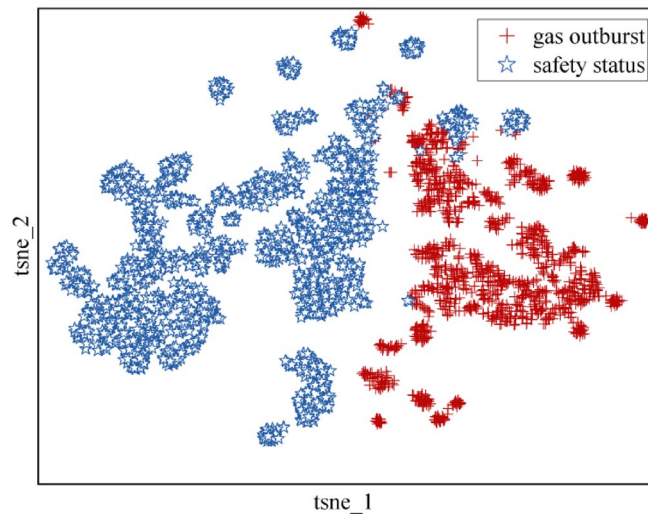


**Fig. 10.** Reduced-dimensional distribution of the t-SNE composite data.

can be misleading, since a model may obtain a high score by predominantly predicting negative labels while failing to detect rare but critical events. Moreover, in multi-type SE classification settings, it is essential to examine not only the overall correctness but also the patterns of misclassification and their potential inter-label dependencies, as these directly affect the reliability of risk assessment. Therefore, three complementary metrics—accuracy, Hamming loss, and ranking loss—are adopted to provide a more comprehensive evaluation of model performance under imbalanced multi-type SE scenarios.

Accuracy is used as an overall metric to assess the overall classification performance of the model. The value domain of the accuracy rate is  $[0,1]$ . Its formula is shown in Eq. (16).

$$\text{Accuracy}(\mathcal{Y}, \hat{\mathcal{Y}}) = \frac{1}{n_{\text{samples}}} \sum_{i=0}^{n_{\text{samples}}-1} 1(\hat{\mathcal{Y}} = \mathcal{Y}) \quad (16)$$

where  $\mathcal{Y} \in \{0, 1\}^{n_{\text{samples}} \times m}$  and  $\hat{\mathcal{Y}} \in \{0, 1\}^{n_{\text{samples}} \times m}$  represent the true and predicted results for each sample, respectively.

The Hamming loss (Hloss) comprehensively considers the misclassification of SEs, i.e., the degree of inconsistency between the predicted and actual results for each SE. This metric provides insight into the classification effectiveness of the tested model. The value domain of the Hamming loss is  $[0, 1]$ .

$$\text{Hloss}(\mathcal{Y}, \hat{\mathcal{Y}}) = \frac{1}{n_{\text{samples}}} \sum_{i=0}^{n_{\text{samples}}-1} \frac{1}{m} |\hat{\mathcal{Y}} \Delta \mathcal{Y}| \quad (17)$$

where  $\Delta$  represents the symmetry difference between two sets, and  $m$  is the total number of SEs.

The ranking loss (Rloss) is used to assess the accuracy of the model when ranking the severity of SE occurrences. The value domain of the ranking loss is  $[0, 1]$ .

$$\text{Rloss} = \frac{1}{n_{\text{samples}}} \sum_{i=0}^{n_{\text{samples}}-1} \frac{1}{\|\mathcal{Y}_i\|_0 (m - \|\mathcal{Y}_i\|_0)} \{ |(k, l) : \mathbf{P}_{ik} \leq \mathbf{P}_{il}, \mathcal{Y}_{ik} = 1, \mathcal{Y}_{il} = 0 \} \quad (18)$$

## Results and discussion

Most existing research focuses on analyzing individual events using models such as support vector machines (SVMs), Bayesian methods, and logistic regression (LR). However, relatively few studies have developed comprehensive models for analyzing multitype SEs. This section presents the results of performance analysis experiments conducted on the RIAM for both single-type and multitype SEs. The first experiment evaluates the performance of the RIAM in terms of assessing individual SE to validate the effectiveness of the model in isolated event scenarios. The second experiment simultaneously considers multiple types of SEs to investigate the applicability of the model to complex and diverse contexts. To ensure a fair and unbiased evaluation, all models were trained and tested under the same tenfold cross-validation protocol, as illustrated in Fig. 11.

### Comparative analysis of the individual SEs of 4 models

The SVM, LR, and naive Bayes (NB) methods are selected as baseline models to assess the risk of SEs. SVM is a binary classification model that efficiently classifies data by maximizing the margin between the decision boundary and support vectors<sup>57</sup>. LR is a probability-based classification method that uses a linear combination

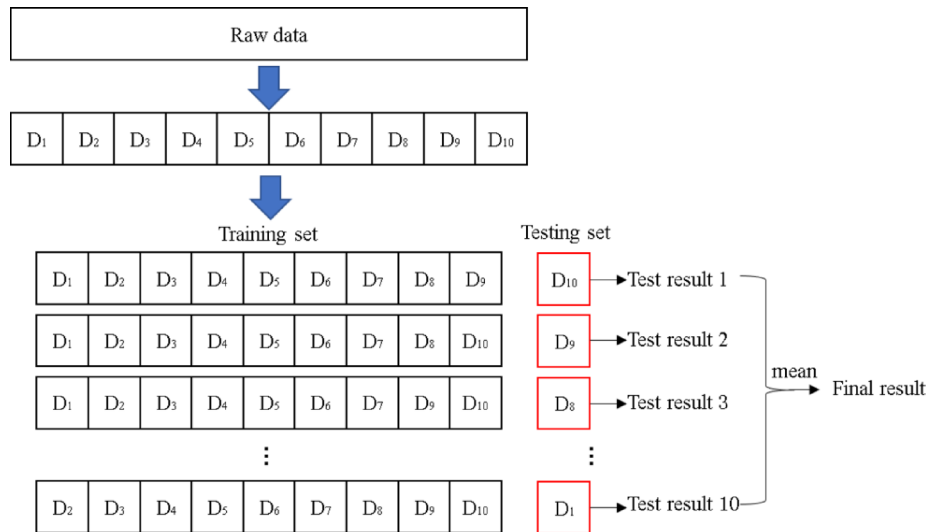


**Fig. 11.** Tenfold cross-validation process.

Model	Hyperparameters	Value
SVM	C	1
	Kernel	Linear
	max_iter	10,000,000
LR	Penalty	L2
	C	1
	Solver	lbfgs
NB	var_smoothing	1e-9
RIAM_Single	Learning rate	0.001
	Batch size	32
	$d_l$	64
	Max_epochs	200
	Optimizer	Adam
	Dropout rate	0.1
	Input dimensions	6
	Output dimensions	1
	Activation function	Sigmoid
	U	2
$N_x$	2	

**Table 3.** The hyperparameters of the proposed method and the baselines.

of the input features and maps the output values to a probability space using a logistic function<sup>45</sup>. NB, based on Bayes’ theorem and the assumption of conditional independence concerning the features in different classes, offers a simple yet effective classification approach<sup>58</sup>. The key parameters of each model are detailed in Table 3.

To comprehensively evaluate the performance of the RIAM model in identifying single safety events ( $s_1-s_3$ ), this study reports the average performance (Mean  $\pm$  Std) of each model under a tenfold cross-validation.

Furthermore, statistical significance tests are introduced to verify whether the performance improvements are reliable and reproducible. Since the test results of different models on the same fold form naturally paired samples in the tenfold cross-validation, the Wilcoxon signed-rank test is used to assess the significance of the differences between RIAM and each baseline model (LR, NB, SVM). This test does not rely on the normality assumption of the differences and is suitable for scenarios with small sample sizes ( $n = 10$ ) and potentially skewed performance distributions. It evaluates whether the median difference in model performance is significantly greater than zero.

To avoid inflation of Type I errors due to multiple comparisons, Holm-Bonferroni correction is applied to adjust the p-values, and the Holm-adjusted p-value ( $p_{adj}$ ) is used as the criterion for statistical significance. In addition to statistical significance, this study further reports two effect size metrics to avoid situations where a “significant p-value” might correspond to negligible improvements:

Cohen's  $d_z$ : This is a standardized effect size for paired tests, defined as the mean difference in performance across folds divided by the standard deviation of the differences. It measures the “stability and strength” of the improvement.

Cliff's  $\delta$ : A non-parametric effect size that is independent of the distribution, it measures the degree of “dominance” of RIAM over the baseline in fold-level performance. When  $\delta$  approaches 1, it indicates that RIAM outperforms the comparison model on nearly every fold.

To maintain consistency in interpreting effect sizes, standard thresholds are used: for Cohen's  $d_z$ , a  $d_z \geq 0.8$  is generally considered a large effect, while for Cliff's  $\delta$ ,  $\delta > 0.474$  is typically interpreted as a large effect<sup>59,60</sup>. The results show that RIAM consistently achieves  $d_z$  values well above 0.8, with  $\delta$  values close to 1, indicating that the performance improvements not only have statistical significance but also exhibit high consistency and stability at the fold level. Therefore, categorizing the effect sizes as large is both reasonable and conservative.

For  $s_1$ , RIAM-Single achieves  $0.9890 \pm 0.0056$ , outperforming LR ( $0.9313 \pm 0.0134$ ), NB ( $0.9042 \pm 0.0105$ ), and SVM ( $0.9198 \pm 0.0058$ ), with gains of  $\Delta = +0.0578$ ,  $+0.0848$ , and  $+0.0693$ , respectively. Wilcoxon signed-rank tests with Holm correction confirm statistically significant differences between RIAM and each baseline model, with large effects, indicating highly reproducible improvements.

For  $s_2$ , RIAM-Single obtains  $0.9710 \pm 0.0113$ , with the most pronounced improvement over LR ( $\Delta = +0.1322$ ), while also exceeding NB and SVM by  $\Delta = +0.0390$  and  $\Delta = +0.0530$ , respectively. All comparisons remain significant after Holm adjustment ( $p_{\text{adj}} \leq 0.00293$ ) with large effect sizes, suggesting that RIAM-Single provides more robust discrimination for this rare label.

For  $s_3$ , RIAM-Single reaches  $0.9908 \pm 0.0044$ , significantly outperforming LR and NB ( $p_{\text{adj}} = 0.01855$ ). Although the margin over SVM is smaller ( $\Delta = +0.0071$ ), it remains statistically significant ( $p_{\text{adj}} = 0.01855$ ) with a medium effect size ( $d_z = 0.789$ ;  $\delta = 0.46$ ), indicating that SVM is already competitive on this label while RIAM-Single still provides stable gains.

Beyond accuracy, Fig. 12 illustrates the overall performance from an accuracy–deviation trade-off perspective. RIAM-Single consistently falls into a favorable region with high accuracy and low-to-moderate deviation, indicating that the performance improvement is achieved without introducing excessive fold-to-fold variability. By contrast, baseline models either suffer from reduced accuracy or exhibit larger deviation fluctuations across labels, implying higher sensitivity to data splits and weaker robustness. Taken together, Table 4 and Fig. 12 provide strong evidence that RIAM-Single delivers statistically significant, reproducible, and robust improvements in individual SE identification.

#### Comprehensive risk analysis of multiple types of SEs

In practical coal mine safety scenarios, multiple types of SEs may co-occur under the same environmental conditions and exhibit coupled behaviors. However, many conventional risk assessment approaches implicitly assume mutual exclusivity among different SE types, which limits their applicability in real-world underground safety systems. To address this issue, the comprehensive risk analysis problem is formulated as a multi-label classification task, where each sample may be associated with multiple SE labels, enabling concurrent identification and joint evaluation of heterogeneous SE risks.

To validate the effectiveness of RIAM\_Multi in comprehensive multi-type SE identification, four representative multi-label baselines are selected:

Classifier Chain (CC): a classic multi-label strategy that models label dependencies sequentially. While it captures conditional correlations across labels, it is sensitive to chain order and may suffer from error propagation.

Extremely Randomized Trees (ExtraTrees): an ensemble-based nonlinear classifier with strong robustness and fitting capability, serving as a competitive traditional machine learning baseline.

Multi-gate Mixture-of-Experts (MMOE): a typical multi-task/multi-label architecture that combines shared experts and gated task-specific fusion, widely adopted for multi-label prediction.

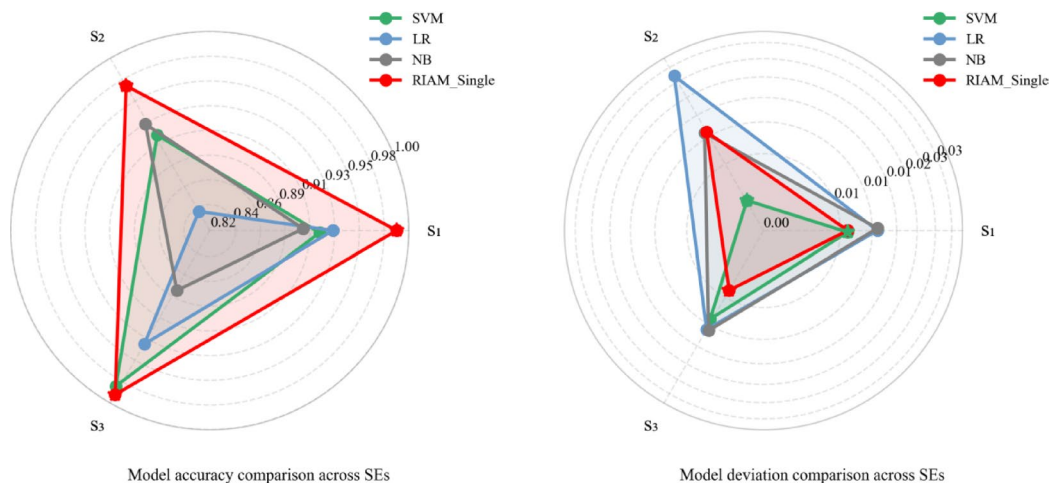


**Fig. 12.** Accuracy and deviation comparison of SE risk assessment across models.

Label	Comparison	RIAM (Mean $\pm$ Std)	Baseline (Mean $\pm$ Std)	$\Delta$ Mean	Holm-adjusted p	Cohen's dz	Cliff's $\delta$	Effect
$s_1$	RIAM vs LR	<b>0.9890 <math>\pm</math> 0.0056</b>	0.9313 $\pm$ 0.0134	0.0578	0.00293 (**)	4.74	1	Large
$s_1$	RIAM vs NB	<b>0.9890 <math>\pm</math> 0.0056</b>	0.9042 $\pm$ 0.0105	0.0848	0.00195 (**)	9.008	1	Large
$s_1$	RIAM vs SVM	<b>0.9890 <math>\pm</math> 0.0056</b>	0.9198 $\pm$ 0.0058	0.0693	0.00098 (***)	8.838	1	Large
$s_2$	RIAM vs LR	<b>0.9710 <math>\pm</math> 0.0113</b>	0.8388 $\pm$ 0.0274	0.1322	0.00293 (**)	4.5	1	Large
$s_2$	RIAM vs NB	<b>0.9710 <math>\pm</math> 0.0113</b>	0.9320 $\pm$ 0.0114	0.039	0.00195 (**)	3.479	0.98	Large
$s_2$	RIAM vs SVM	<b>0.9710 <math>\pm</math> 0.0113</b>	0.9180 $\pm$ 0.0011	0.053	0.00098 (***)	4.617	1	Large
$s_3$	RIAM vs LR	<b>0.9908 <math>\pm</math> 0.0044</b>	0.9376 $\pm$ 0.0108	0.0532	0.01855 (*)	3.905	1	Large
$s_3$	RIAM vs NB	<b>0.9908 <math>\pm</math> 0.0044</b>	0.8811 $\pm$ 0.0107	0.1098	0.01855 (*)	9.595	1	Large
$s_3$	RIAM vs SVM	<b>0.9908 <math>\pm</math> 0.0044</b>	0.9837 $\pm$ 0.0086	0.0071	0.01855 (*)	0.789	0.46	Medium

**Table 4.** Statistical significance testing of RIAM against baseline models (tenfold CV).

Multi-layer Perceptron (MLP): a standard deep feed-forward network used to evaluate the gain brought by nonlinear representation learning and provide a lightweight deep learning baseline.

These baselines cover major paradigms in multi-label learning, including sequential label-dependency modeling, ensemble-based nonlinear learning, mixture-of-experts architectures, and standard deep feed-forward modeling. The compared models and hyperparameter settings are summarized in Table 5. All methods were trained and evaluated under the same cross-validation protocol and data preprocessing pipeline to ensure fair comparison.

Figure 13 compares the fold-wise performance distributions of the compared models under tenfold cross-validation, including accuracy, Hamming loss, and ranking loss. RIAM exhibits consistently superior and stable performance, achieving the highest accuracy and simultaneously yielding the lowest Hamming loss, while maintaining a near-zero ranking loss. The compact violin distributions further indicate reduced inter-fold variance, suggesting enhanced generalization and reliability under data-scarce and imbalanced SE scenarios. In particular, the near-zero ranking loss indicates that RIAM can provide reliable risk ordering, which is critical for prioritizing early-warning responses when multiple SEs co-occur. In contrast, CC presents noticeable performance degradation with larger fluctuations, while ExtraTrees, MMOE, and MLP remain competitive but are overall outperformed by RIAM.

As summarized in Table 6, RIAM\_Multi achieves the best overall performance across the SE set, obtaining an accuracy of  $0.9554 \pm 0.0129$  and the lowest Hamming loss of  $0.0162 \pm 0.0049$ . Compared with CC, ExtraTrees, MMOE, and MLP, RIAM\_Multi yields consistent improvements in accuracy ( $\Delta = +0.1459, +0.0690, +0.0519$ , and  $+0.0260$ , respectively), while simultaneously reducing per-label misclassification rate. These results confirm that RIAM\_Multi is capable of accurately identifying co-occurring SEs in an imbalanced multi-event setting.

To further ensure that the observed improvements are not attributable to random data splits, paired Wilcoxon signed-rank tests with Holm correction were conducted on the two primary metrics (accuracy and Hamming loss). Statistically significant improvements are observed across all comparisons ( $p_{\text{adj}} \leq 0.0049$ ). Moreover, the improvements are accompanied by large effect sizes (Cohen's  $d \geq 1.14$ , Cliff's  $\delta \geq 0.83$ ), indicating that RIAM not only improves average performance but also maintains consistent superiority across folds. Notably,  $\delta$  values approaching 1.0 suggest that RIAM outperforms competing methods in nearly all folds, demonstrating strong robustness under co-occurring and imbalanced SE conditions.

To evaluate the reliability of RIAM\_Multi at the level of individual SE types, the confusion matrices for each SE are further reported in Fig. 14. A clear dominance of diagonal entries can be observed, indicating high agreement between the predicted labels and ground-truth outcomes. This result suggests that RIAM\_Multi preserves stable discriminative capability for each SE type, even under multi-label co-occurrence conditions.

Overall, RIAM achieves improved accuracy in risk identification and assessment tasks, while providing a comprehensive evaluation for multiple SE types under co-occurrence conditions. The advantages of RIAM primarily originate from two aspects. First, the model explicitly considers the correlations among multiple environmental factors (MEFs), which helps capture coupled risk patterns in underground environments. Second, RIAM differentiates the contributions of MEFs to SEs, enabling a more faithful representation of factor-driven mechanisms and improving the interpretability of identification outcomes. In addition, RIAM exhibits limited dependence on specific production conditions (e.g., ventilation modes), demonstrating robustness in similar engineering contexts and supporting its applicability and generalization in real-world coal mine scenarios.

#### Interpretability analysis

The proposed model demonstrates high stability and reliability in the integrated identification of multiple SEs. This performance can be largely attributed to its strong interpretability, which facilitates understanding of internal mechanisms and integration of key information related to SEs. The interpretability analysis is conducted from two complementary perspectives:

##### (1) Correlation between MEFs.

By modeling the correlations among MEFs, the proposed model identifies latent coupling relationships and synergistic patterns across multiple data sources. Specifically, the key information capture module learns inter-factor interactions through correlation-weight learning (Eq. (8)), resulting in informative MEF embeddings. Let  $\mathcal{X}^{N_x} \in \mathbb{R}^{f \times d_l}$  denote the  $N_x$ -th layer output of the key information capture module, where  $\mathcal{X}_i^{N_x} \in \mathbb{R}^{d_l}$

Model	Hyperparameters	Value
CC	C	1
	Solver	liblinear
	Class weight	balanced
	Max_iter	2000
	Chain order	random (order = None)
ExtraTrees	n_estimators	500
	max_depth	None
	min_samples_split	2
	min_samples_leaf	1
	max_features	sqrt
MMoE	Learning rate	0.001
	Batch size	32
	Max_epochs	100
	Optimizer	Adam
	Dropout	0.1
	Num experts	4
	Expert out dim	32
	Expert hidden dim	64
	Tower hidden dim	64
	Activation functions	ReLU (experts/towers), Sigmoid (output)
MLP	Learning rate	0.001
	Batch size	64
	Hidden dim	64
	Max_epochs	150
	Optimizer	Adam
	Dropout	0.2
	Activation functions	GELU (backbone), Sigmoid (output)
RIAM_Multi	Learning rate	0.001
	Batch size	32
	dl	64
	Max_epochs	200
	Optimizer	Adam
	Dropout	0.1
	Input dimensions	6
	Output dimensions	3
	Activation functions	Sigmoid
	U	2
	N <sub>x</sub>	2

**Table 5.** Compared models and hyperparameter settings for multi-label SE identification.

represents the embedding vector of the  $i$ -th MEF. To visualize the learned dependency structure, the MEF correlation matrix is computed based on the absolute cosine similarity between MEF embeddings:

$$\hat{C}_{ij} = \frac{\mathbf{x}_i^{N_x} \cdot \mathbf{x}_j^{N_x}}{\|\mathbf{x}_i^{N_x}\| \|\mathbf{x}_j^{N_x}\|} \quad (19)$$

$$\mathbf{C}_{ij} = |\hat{C}_{ij}|$$

As illustrated in Fig. 15, the resulting correlation matrix reveals distinct interrelationships among environmental parameters, exhibiting clear variations in coupling strengths across different MEFs. Overall, these results demonstrate that the proposed model can effectively uncover complex multi-factor dependency structures and coevolutionary patterns within the mine environment, providing interpretability support for subsequent MEF-SE contribution analysis.

(2) Contribution of MEFs to SEs.

To further interpret how different MEFs contribute to the occurrence of multiple SEs, the MEF-SE mapping weights learned by the cross-scale mapping module are analyzed. Specifically, the module constructs an event-aware contribution matrix  $\beta \in \mathbb{R}^{m \times f}$ , where  $m$  and  $f$  denote the number of SE types and MEFs, respectively.

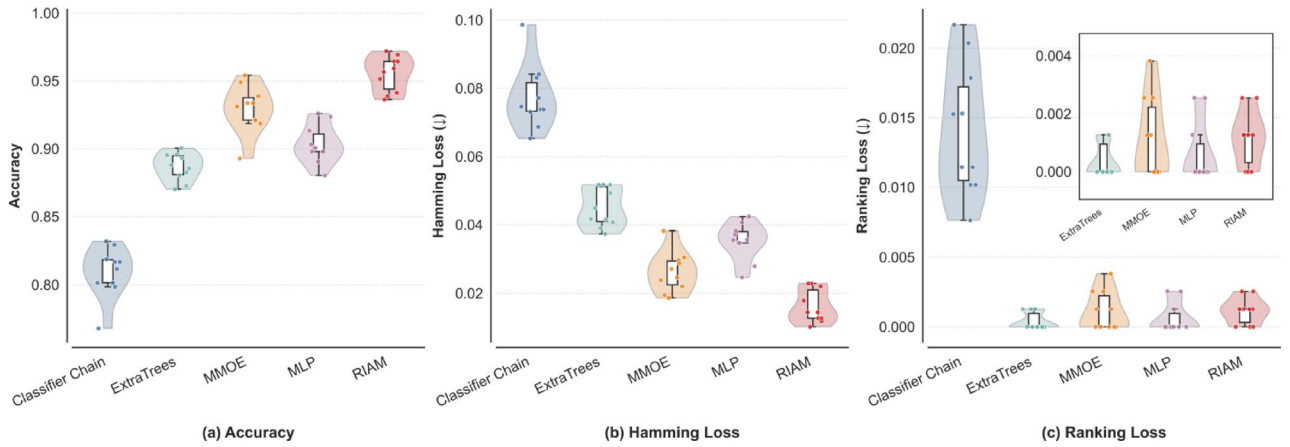


**Fig. 13.** Performance distribution comparison of multi-label SE risk identification under tenfold cross-validation.

Metric	Comparison	RIAM (Mean ± Std)	Baseline (Mean ± Std)	ΔMean	Holm-adj. p	Cohen's dz	Cliff's δ	Effect
Accuracy (+)	RIAM vs Classifier Chain	<b>0.9554 ± 0.0129</b>	0.8095 ± 0.0185	0.1459	0.0039(**)	6.9715	1	Large
	RIAM vs ExtraTrees	<b>0.9554 ± 0.0129</b>	0.8864 ± 0.0101	0.069	0.0039(**)	5.4329	1	Large
	RIAM vs MMOE	<b>0.9554 ± 0.0129</b>	0.9035 ± 0.0141	0.0519	0.0039(**)	3.7383	1	Large
	RIAM vs MLP	<b>0.9554 ± 0.0129</b>	0.9295 ± 0.0174	0.026	0.0049(**)	1.142	0.83	Large
Hloss (-)	RIAM vs Classifier Chain	<b>0.0162 ± 0.0049</b>	0.0772 ± 0.0094	-0.061	0.0039(**)	6.3099	1	Large
	RIAM vs ExtraTrees	<b>0.0162 ± 0.0049</b>	0.0450 ± 0.0057	-0.0288	0.0039(**)	4.7617	1	Large
	RIAM vs MMOE	<b>0.0162 ± 0.0049</b>	0.0352 ± 0.0054	-0.019	0.0039(**)	3.2565	1	Large
	RIAM vs MLP	<b>0.0162 ± 0.0049</b>	0.0263 ± 0.0059	-0.0101	0.0049(**)	1.1945	0.83	Large

**Table 6.** Performance comparison between RIAM and baseline models (tenfold cross-validation).

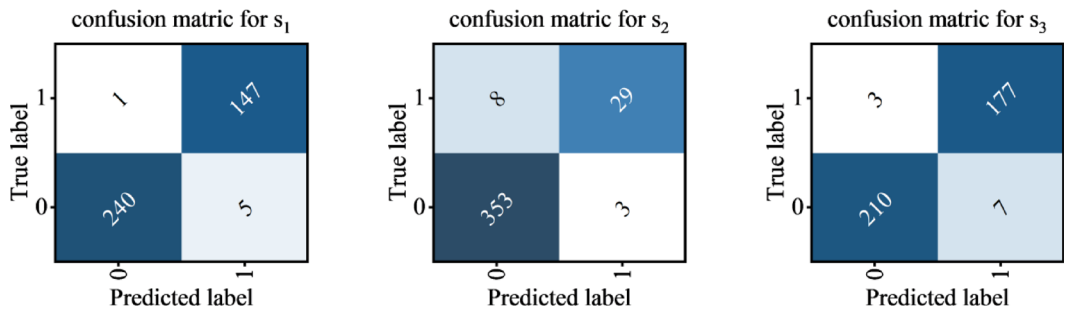


**Fig. 14.** The confusion matrix produced by the RIAM for each SE classification task.

Each element  $\beta_{jk}$  quantifies the relative contribution of the  $j$ -th MEF to the  $k$ -th safety event. The computation of  $\beta$  follows Eq. (11). It is row-normalized by design, satisfying:

$$\sum_{j=1}^f \beta_{jk} = 1, k = 1, 2, \dots, m \tag{20}$$

Different SEs correspond to distinct coupling pathways among MEFs. To characterize such differences, the cross-scale mapping module provides event-specific contribution distributions, thereby enabling differentiated interpretation for each event type. The resulting contribution degrees are shown in Figs. 16, 17 and 18. For  $s_1$ , the contribution ranking of MEFs is:  $\beta_{31} > \beta_{51} > \beta_{61} > \beta_{41} > \beta_{11}$ . For  $s_2$ , the contribution ranking is:  $\beta_{12} > \beta_{52} > \beta_{62} > \beta_{42} > \beta_{22} > \beta_{32}$ . For  $s_3$ , the contribution ranking is:  $\beta_{33} > \beta_{23} > \beta_{43} > \beta_{53} > \beta_{13} > \beta_{63}$ . These results verify the model's capability for differentiated identification within a multi-event integrated recognition framework, indicating that the model can effectively separate the characteristic representations of different SEs.

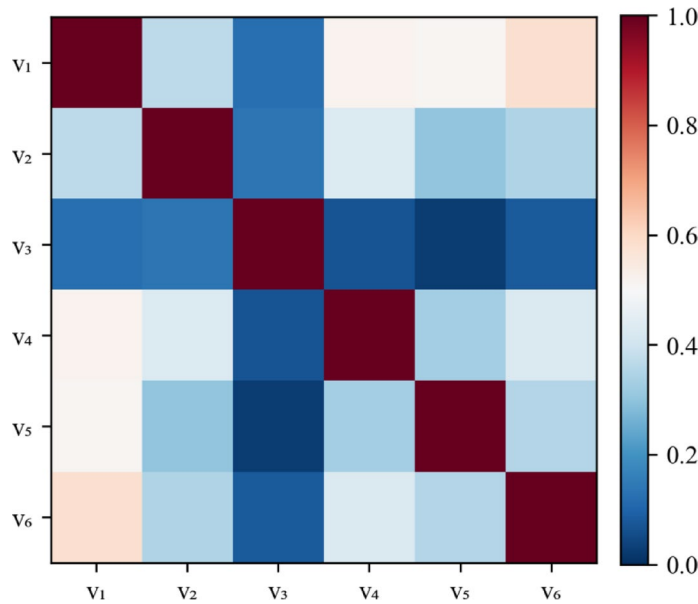


Fig. 15. Inter-factor Correlation Matrix among MEFs.

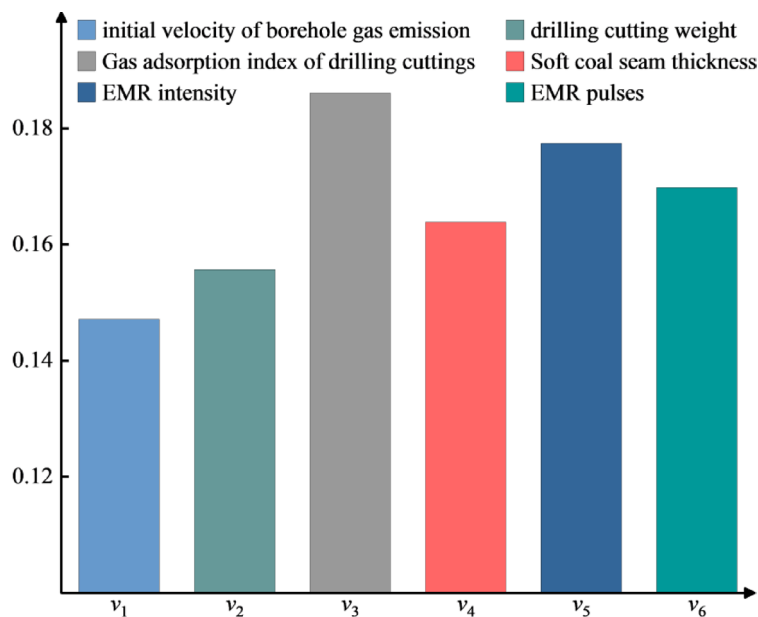


Fig. 16. MEFs contribution Map for  $s_1$ .

The quantified contribution scores are further used to dynamically weight MEF feature representations, enabling the model to emphasize influential factors while reducing the impact of less relevant ones. This mechanism allows the model to achieve differentiated identification of multiple SEs and to prioritize key influencing factors. The model’s interpretability improves prediction accuracy, strengthens the utilization of critical information, and enhances the stability, reliability, and transparency of decision-making.

### Conclusions

In this study, a theoretical model based on the occurrence mechanism of safety events (SEs) is used as a fundamental framework and is deeply integrated with the data-driven risk identification and analysis model (RIAM), to establish a theoretically and practically integrated analysis model. At the theoretical level, a cross-scale emergent mechanism for mapping environmental factors to SEs is established. Accordingly, a data-driven RIAM is constructed. Thus, an intelligent SE analysis model is proposed, providing causative tracing, environmental factor preference identification, and comprehensive analytical capability. The main conclusions are as follows.

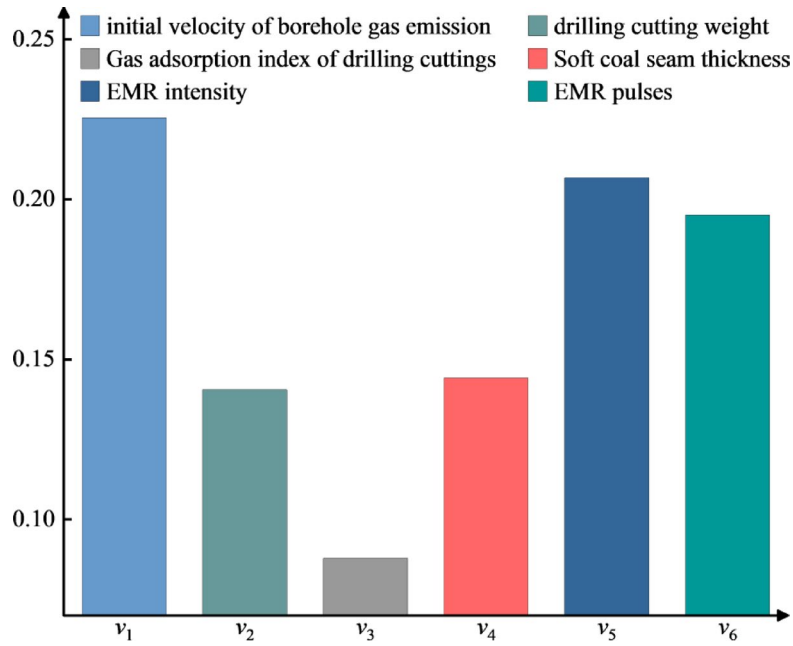


Fig. 17. MEFs contribution Map for  $s_2$ .

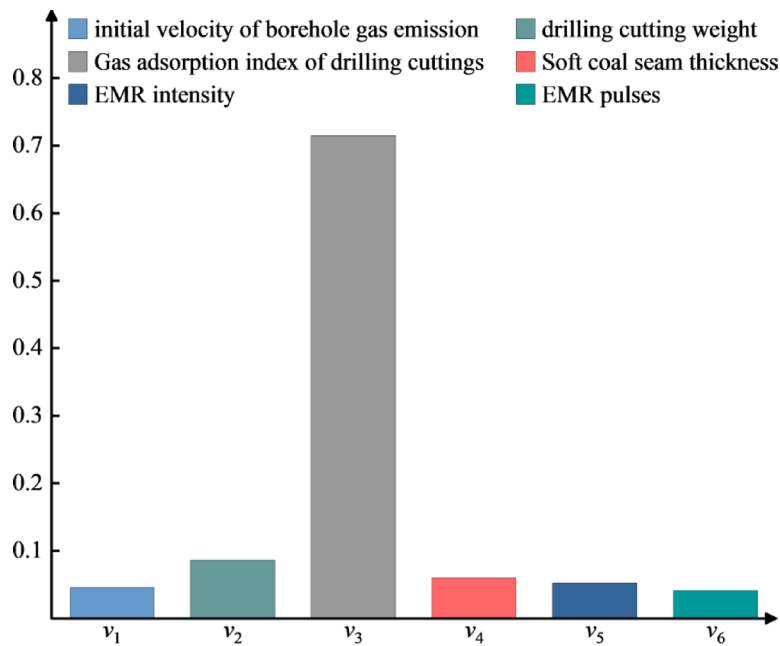


Fig. 18. MEFs contribution Map for  $s_3$ .

1. SEs demonstrate cross-level and cross-scale emergence due to the nonlinear coupling of environmental factors. At the factor scale, the states of the associated environmental factors exhibit dynamic, interactive influences and updating mechanisms. As the underlying environmental factors that can be obtained, measurable environmental factors (MEFs) provide reliable data support for SE analysis tasks. At the event scale, SEs interact in a dynamic chain, intertwining and superimposing on one another. With respect to the cross-scale emergence mechanism for mapping MEFs to SEs, the contributions of MEFs to SEs vary. This variation not only enables the identification of the key environmental factors but also affects the precision of SE analyses.
2. The proposed RIAM is grounded in theoretical research and can comprehensively identify and evaluate multitype SE risks. Compared to LR, SVM, and NB, the RIAM significantly enhances the accuracy of its SE analysis results while ensuring high risk analysis accuracy on an SE set. Moreover, the interpretability of the

model allows for learning the contributions of the MEFs to the SEs online, enhancing its practical applicability in dynamic environments.

The theoretical model and the mathematical risk analysis model constructed in this study form a complementary analytical framework. However, this study has several limitations. Although the RIAM possesses certain self-learning capabilities, its performance is highly dependent on the quality and quantity of the available data. When the input data are incomplete or insufficient, the accuracy of the analysis results may be adversely affected. To address this limitation, future research should consider integrating prior SE link relationship knowledge as auxiliary information into the RIAM. This approach can provide additional guidance and constraints for the model, thereby partially mitigating the issues related to insufficient or poor-quality data.

## Data availability

The data that support the findings of this study are available from the corresponding author upon reasonable request.

Received: 3 December 2025; Accepted: 9 February 2026

Published online: 16 February 2026

## References

- Huang, L., Wu, C. & Wang, B. Challenges, opportunities and paradigm of applying big data to production safety management: From a theoretical perspective. *J. Clean. Prod.* **231**, 592–599. <https://doi.org/10.1016/j.jclepro.2019.05.245> (2019).
- Huang, L., Wu, C., Wang, B. & Ouyang, Q. A new paradigm for accident investigation and analysis in the era of big data. *Proc. Saf. Prog.* **37**, 42–48. <https://doi.org/10.1002/prs.11898> (2018).
- Ouyang, Q., Wu, C. & Huang, L. Methodologies, principles and prospects of applying big data in safety science research. *Saf. Sci.* **101**, 60–71. <https://doi.org/10.1016/j.ssci.2017.08.012> (2018).
- Huang, L., Wu, C., Wang, B. & Ouyang, Q. Big-data-driven safety decision-making: A conceptual framework and its influencing factors. *Saf. Sci.* **109**, 46–56. <https://doi.org/10.1016/j.ssci.2018.05.012> (2018).
- Wang, B., Wang, Y., Yan, F. & Zhao, W. Safety intelligence toward safety management in a big-data environment: A general model and its application in urban safety management. *Saf. Sci.* **154**, 105840. <https://doi.org/10.1016/j.ssci.2022.105840> (2022).
- Wang, B., Yun, M., Liu, Q. & Wang, Y. Precision safety management (PSM): A novel and promising approach to safety management in the precision era. *Saf. Sci.* **157**, 105931. <https://doi.org/10.1016/j.ssci.2022.105931> (2023).
- Wang, Y. et al. Establishment of safety structure theory. *Saf. Sci.* **115**, 265–277. <https://doi.org/10.1016/j.ssci.2019.02.013> (2019).
- Wang, Y., Deng, C., Jin, Z., Liu, Q. & Qiao, L. Definition and mathematical expression on instability domain of safety event and safety structure. *Process Saf. Environ. Prot.* **156**, 57–71. <https://doi.org/10.1016/j.psep.2021.09.045> (2021).
- Du, P. et al. Risk assessment and defense resource allocation optimization for mining cyber-physical systems under coordinated attacks. *Comput. Secur.* **160**, 104741. <https://doi.org/10.1016/j.cose.2025.104741> (2026).
- Niu, Y., Fan, Y. & Ju, X. Critical review on data-driven approaches for learning from accidents: Comparative analysis and future research. *Saf. Sci.* **171**, 106381. <https://doi.org/10.1016/j.ssci.2023.106381> (2024).
- Liang, C. et al. Escalation probabilistic model of atmospheric tank under coupling effect of thermal radiation and blast wave in domino accidents. *J. Loss Prev. Process Ind.* **80**, 104888. <https://doi.org/10.1016/j.jlp.2022.104888> (2022).
- Feng, J. R., Yu, G., Zhao, M., Zhang, J. & Lu, S. Dynamic risk assessment framework for industrial systems based on accidents chain theory: The case study of fire and explosion risk of UHV converter transformer. *Reliab. Eng. Syst. Saf.* **228**, 108760. <https://doi.org/10.1016/j.res.2022.108760> (2022).
- Muduli, L., Jana, P. K. & Mishra, D. P. Wireless sensor network based fire monitoring in underground coal mines: A fuzzy logic approach. *Process Saf. Environ. Prot.* **113**, 435–447. <https://doi.org/10.1016/j.psep.2017.11.003> (2018).
- Du, J. et al. Risk assessment of dynamic disasters in deep coal mines based on multi-source, multi-parameter indexes, and engineering application. *Process Saf. Environ. Prot.* **155**, 575–586. <https://doi.org/10.1016/j.psep.2021.09.034> (2021).
- Fu, G. et al. The development history of accident causation models in the past 100 years: 24Model, a more modern accident causation model. *Process Saf. Environ. Prot.* **134**, 47–82. <https://doi.org/10.1016/j.psep.2019.11.027> (2020).
- Wang, X., Wang, L., Chen, X., Ning, R. & Zhou, J. Joint optimization of protection adjustment and preventive maintenance policies for multi-state self-healing systems with protective devices in a shock environment. *Reliab. Eng. Syst. Saf.* **269**, 112000. <https://doi.org/10.1016/j.res.2025.112000> (2026).
- Xu, Y., Reniers, G., Yang, M., Yuan, S. & Chen, C. Uncertainties and their treatment in the quantitative risk assessment of domino effects: Classification and review. *Process Saf. Environ. Prot.* **172**, 971–985. <https://doi.org/10.1016/j.psep.2023.02.082> (2023).
- Salmon, P. M., Cornelissen, M. & Trotter, M. J. Systems-based accident analysis methods: A comparison of Accimap, HFACS, and STAMP. *Saf. Sci.* **50**, 1158–1170. <https://doi.org/10.1016/j.ssci.2011.11.009> (2012).
- Fukuoka, K. Visualization of a hole and accident preventive measures based on the Swiss cheese model developed by risk management and process approach. *WMU J. Marit. Aff.* **15**, 127–142. <https://doi.org/10.1007/s13437-015-0076-2> (2016).
- Chen, Y. & Wang, Z. Accident causing theory in construction safety management. *IOP Conf. Ser. Earth Environ. Sci.* **638**, 012097. <https://doi.org/10.1088/1755-1315/638/1/012097> (2021).
- Hollnagel, E. Understanding accidents-from root causes to performance variability. In: Proceedings of the IEEE 7th Conference on Human Factors and Power Plants, Scottsdale, AZ, USA, p. 1-1-1–6 (IEEE, 2002). <https://doi.org/10.1109/HFPP.2002.1042821>.
- Leveson, N. A new accident model for engineering safer systems. *Saf. Sci.* **42**, 237–270. [https://doi.org/10.1016/S0925-7535\(03\)00047-X](https://doi.org/10.1016/S0925-7535(03)00047-X) (2004).
- Ceylan, B. O., Akyuz, E. & Arslan, O. Systems-theoretic accident model and processes (STAMP) approach to analyse socio-technical systems of ship Allision in narrow waters. *Ocean Eng.* **239**, 109804. <https://doi.org/10.1016/j.oceaneng.2021.109804> (2021).
- Wu, Y. et al. A popular systemic accident model in China: Theory and applications of 24Model. *Saf. Sci.* **159**, 106013. <https://doi.org/10.1016/j.ssci.2022.106013> (2023).
- Du, P., Wang, X., Li, T., Su, C. & Li, Z. Resilience optimization analysis of smart mining cluster cyber-physical systems based on the NK model. *Process Saf. Environ. Prot.* **192**, 321–330. <https://doi.org/10.1016/j.psep.2024.10.078> (2024).
- Du, P., Wang, X., Li, T., Su, C. & Zhu, J. Research on cross-space risk transfer mechanism of mine cyber-physical fusion system in the context of smart mining. In: Proceedings of the Institution of Mechanical Engineers, Part O: Journal of Risk and Reliability 1748006X251348335 (2025). <https://doi.org/10.1177/1748006X251348335>.
- Johnson, W. G. MORT safety assurance systems 1980.
- Wang, Y., Li, P., Hong, C. & Yang, Z. Causation analysis of ship collisions using a TM-FRAM model. *Reliab. Eng. Syst. Saf.* **260**, 111035. <https://doi.org/10.1016/j.res.2025.111035> (2025).

29. Qian, X. & Chen, B. Catastrophe model of accident causation. *China Saf. Sci. J.* <https://doi.org/10.16265/j.cnki.issn1003-3033.1995.02.001> (1995).
30. Li, K. & Wang, S. A network accident causation model for monitoring railway safety. *Saf. Sci.* **109**, 398–402. <https://doi.org/10.1016/j.ssci.2018.06.008> (2018).
31. Li, M., Wang, H., Wang, D., Shao, Z. & He, S. Risk assessment of gas explosion in coal mines based on fuzzy AHP and Bayesian network. *Process Saf. Environ. Prot.* **135**, 207–218. <https://doi.org/10.1016/j.psep.2020.01.003> (2020).
32. Zhang, L., Wu, X., Skibniewski, M. J., Zhong, J. & Lu, Y. Bayesian-network-based safety risk analysis in construction projects. *Reliab. Eng. Syst. Saf.* **131**, 29–39. <https://doi.org/10.1016/j.res.2014.06.006> (2014).
33. Feng, J. R., Zhao, M., Yu, G., Zhang, J. & Lu, S. Dynamic risk analysis of accidents chain and system protection strategy based on complex network and node structure importance. *Reliab. Eng. Syst. Saf.* **238**, 109413. <https://doi.org/10.1016/j.res.2023.109413> (2023).
34. Zhang, L., Cai, S. & Hu, J. An adaptive pre-warning method based on trend monitoring: Application to an oil refining process. *Measurement* **139**, 163–176. <https://doi.org/10.1016/j.measurement.2019.03.013> (2019).
35. Wang, E., Li, Z., He, X. & Chen, L. Application and pre-warning technology of coal and gas outburst by electromagnetic radiation. *Coal Sci. Technol.* **42**, 53–57. <https://doi.org/10.13199/j.cnki.cst.2014.06.011> (2014).
36. Wang, R., Chen, S., Li, X., Tian, G. & Zhao, T. AdaBoost-driven multi-parameter real-time warning of rock burst risk in coal mines. *Eng. Appl. Artif. Intell.* **125**, 106591. <https://doi.org/10.1016/j.engappai.2023.106591> (2023).
37. Li, B. et al. Optimize the early warning time of coal and gas outburst by multi-source information fusion method during the tunneling process. *Process Saf. Environ. Prot.* **149**, 839–849. <https://doi.org/10.1016/j.psep.2021.03.029> (2021).
38. Guo, K. & Zhang, L. Multi-source information fusion for safety risk assessment in underground tunnels. *Knowl.-Based Syst.* **227**, 107210. <https://doi.org/10.1016/j.knosys.2021.107210> (2021).
39. Shen, S.-L., Lin, S.-S. & Zhou, A. A cloud model-based approach for risk analysis of excavation system. *Reliab. Eng. Syst. Saf.* **231**, 108984. <https://doi.org/10.1016/j.res.2022.108984> (2023).
40. Guo, X., Fu, G., Hao, C. & Kong, Q. The relationship between “event” and “acts” in the 24 model. *Saf. Secur.* **41**, 44–48. <https://doi.org/10.19737/j.cnki.issn1002-3631.2020.03.008> (2020).
41. Shu, L. et al. A novel physical model of coal and gas outbursts mechanism: Insights into the process and initiation criterion of outbursts. *Fuel* **323**, 124305. <https://doi.org/10.1016/j.fuel.2022.124305> (2022).
42. Zhang, G. & Wang, E. Risk identification for coal and gas outburst in underground coal mines: A critical review and future directions. *Gas Sci. Eng.* **118**, 205106. <https://doi.org/10.1016/j.jgsce.2023.205106> (2023).
43. Tang, J. et al. Determination of critical value of an outburst risk prediction index of working face in a coal roadway based on initial gas emission from a borehole and its application: A case study. *Fuel* **267**, 117229. <https://doi.org/10.1016/j.fuel.2020.117229> (2020).
44. Zhang, G., Wang, E., Li, Z. & Qin, B. Risk assessment of coal and gas outburst in driving face based on finite interval cloud model. *Nat. Hazards* **110**, 1969–1995. <https://doi.org/10.1007/s11069-021-05021-z> (2022).
45. Li, Z., Wang, E., Ou, J. & Liu, Z. Hazard evaluation of coal and gas outbursts in a coal-mine roadway based on logistic regression model. *Int. J. Rock Mech. Min. Sci.* **80**, 185–195. <https://doi.org/10.1016/j.ijrmm.2015.07.006> (2015).
46. Wang, C. et al. Study on factors influencing and the critical value of the drilling cuttings weight: an index for outburst risk prediction. *Process Saf. Environ. Prot.* **140**, 356–366. <https://doi.org/10.1016/j.psep.2020.05.027> (2020).
47. Xue, S., Wang, Y., Xie, J. & Wang, G. A coupled approach to simulate initiation of outbursts of coal and gas—Model development. *Int. J. Coal Geol.* **86**, 222–230. <https://doi.org/10.1016/j.coal.2011.02.006> (2011).
48. Wang, W., Wang, H., Zhang, B., Wang, S. & Xing, W. Coal and gas outburst prediction model based on extension theory and its application. *Process Saf. Environ. Prot.* **154**, 329–337. <https://doi.org/10.1016/j.psep.2021.08.023> (2021).
49. Lama, R. D. & Bodziony, J. Management of outburst in underground coal mines. *Int. J. Coal Geol.* **35**, 83–115. [https://doi.org/10.1016/S0166-5162\(97\)00037-2](https://doi.org/10.1016/S0166-5162(97)00037-2) (1998).
50. Zhai, C., Xiang, X., Xu, J. & Wu, S. The characteristics and main influencing factors affecting coal and gas outbursts in Chinese Pingdingshan mining region. *Nat. Hazards* **82**, 507–530. <https://doi.org/10.1007/s11069-016-2195-2> (2016).
51. Wang, E., He, X., Wei, J., Nie, B. & Song, D. Electromagnetic emission graded warning model and its applications against coal rock dynamic collapses. *Int. J. Rock Mech. Min. Sci.* **48**, 556–564. <https://doi.org/10.1016/j.ijrmm.2011.02.006> (2011).
52. Qiu, L. et al. Characteristics and precursor information of electromagnetic signals of mining-induced coal and gas outburst. *J. Loss Prev. Process. Ind.* **54**, 206–215. <https://doi.org/10.1016/j.jlpi.2018.04.004> (2018).
53. Qiao, W. & Chen, X. Connotation, characteristics and framework of coal mine safety big data. *Heliyon* **8**, e11834. <https://doi.org/10.1016/j.heliyon.2022.e11834> (2022).
54. Zhang, E., Zhou, B., Yang, L., Li, C. & Li, P. Experimental study on the microseismic response characteristics of coal and gas outbursts. *Process Saf. Environ. Prot.* **172**, 1058–1071. <https://doi.org/10.1016/j.psep.2023.02.089> (2023).
55. Ji, Y. et al. Multivariate global agricultural drought frequency analysis using kernel density estimation. *Ecol. Eng.* **177**, 106550. <https://doi.org/10.1016/j.ecoleng.2022.106550> (2022).
56. Najim, S. A. & Lim, I. S. Trustworthy dimension reduction for visualization different data sets. *Inf. Sci.* **278**, 206–220. <https://doi.org/10.1016/j.ins.2014.03.048> (2014).
57. Lai, Z., Liang, G., Zhou, J., Kong, H. & Lu, Y. A joint learning framework for optimal feature extraction and multi-class SVM. *Inf. Sci.* **671**, 120656. <https://doi.org/10.1016/j.ins.2024.120656> (2024).
58. Zeng, Z. & Zio, E. A classification-based framework for trustworthiness assessment of quantitative risk analysis. *Saf. Sci.* **99**, 215–226. <https://doi.org/10.1016/j.ssci.2017.04.001> (2017).
59. Romano, J. & Kromrey, J. Appropriate statistics for ordinal level data: Should we really be using t-test and Cohen's d for evaluating group differences on the NSSE and other Surveys? 2006.
60. Macbeth, G., Razumiejczyk, E. & Ledesma, R. D. Cliff's delta calculator: A non-parametric effect size program for two groups of observations. *Univ. Psychol.* **10**, 545–555. <https://doi.org/10.11144/Javeriana.upsy10-2.cdcp> (2010).

## Author contributions

Conceptualization, Zhixin Jin and Qian Liu; methodology, Junqiao Li and Qian Liu; software, Junqiao Li and Qian Liu; validation, Qian Liu; formal analysis, Qian Liu; investigation, Qian Liu; resources, Junqiao Li and Qian Liu; data curation, Junqiao Li and Qian Liu; writing—original draft preparation, Qian Liu; writing—review and editing, Qian Liu; visualization, Qian Liu; supervision, Junqiao Li and Qian Liu; Project administration, Junqiao Li; Funding acquisition, Junqiao Li.

## Funding

This work was supported by the National Natural Science Foundation of China (No. 52404233), and the Special Fund for Science and Technology Innovation Teams of Shanxi Province (No. 202304051001008).

## Declarations

### Competing interests

The authors declare no competing interests.

### Additional information

**Supplementary Information** The online version contains supplementary material available at <https://doi.org/10.1038/s41598-026-39940-3>.

**Correspondence** and requests for materials should be addressed to J.L.

**Reprints and permissions information** is available at [www.nature.com/reprints](http://www.nature.com/reprints).

**Publisher's note** Springer Nature remains neutral with regard to jurisdictional claims in published maps and institutional affiliations.

**Open Access** This article is licensed under a Creative Commons Attribution-NonCommercial-NoDerivatives 4.0 International License, which permits any non-commercial use, sharing, distribution and reproduction in any medium or format, as long as you give appropriate credit to the original author(s) and the source, provide a link to the Creative Commons licence, and indicate if you modified the licensed material. You do not have permission under this licence to share adapted material derived from this article or parts of it. The images or other third party material in this article are included in the article's Creative Commons licence, unless indicated otherwise in a credit line to the material. If material is not included in the article's Creative Commons licence and your intended use is not permitted by statutory regulation or exceeds the permitted use, you will need to obtain permission directly from the copyright holder. To view a copy of this licence, visit <http://creativecommons.org/licenses/by-nc-nd/4.0/>.

© The Author(s) 2026